Fachbereich Ingenieurwissenschaften der Hochschule RheinMain
Studienbereich Physik   Studiengang Angewandte Physik

Masterthesis

zur Erlangung des akademischen Grades Master of Science
mit dem Thema

Understanding cells communication
Low-frequency electric current measurements of cell populations

vorgelegt von

Paul Schlett

Matr.Nr. 271176

am
13. August 2015

Durchgeführt am

Max-Planck-Institut für Polymerforschung

im Arbeitskreis von Prof. Dr. Paul Blom
Ackermannweg 10 // 55128 Mainz

Referent:	Prof. Dr. Andreas Brensing (HSRM)
Projektleiter:	Prof. Dr. Dago de Leeuw (MPIP)
Korreferent:	Dr. Paulo Rocha (MPIP)

Contents

Abstract

Measuring the electrical activity of large and defined populations of cells is current-
ly a major technical challenge to electrophysiology, especially in the picoampere-
range. For this purpose, we developed novel in-house transducers based on thin
gold electrodes on a glass substrate to record the electric current response, termed
bioelectronic activity, of cultured glioma cells and primary neurons *in vitro*. The
transducer was integrated into an ultra low-noise measuring setup, that allowed
the detection of not only prominent electric activity in glioma cancer cells, but al-
so current fluctuations of electrically quiescent cells of non-brain origin (HeLa) in
comparison. Experiments on C6 glioma cells revealed the origin of the obtained
current signals to be dominated by the flow of Na^+ and K^+ ions through their re-
spective voltage-gated ion channels, since the electrical activity can be effectively
abolished using appropriate pharmacological ion channel inhibitors. In a long-term
measurement of a murine primary embryonic neuron population, the evolution of
bioelectronic activity was monitored over 2 weeks. The current signals evolved from
a random, uncoordinated single cell behavior towards a collaborative, coordinated
and synchronous bioelectronic activity, which is expected to occur only in mature
neuronal networks. The formation of a neuronal network was confirmed by means of
bioelectronic signal analysis in time and frequency domain and optical microscopy.
Thus, we offer here a unique approach for studying electrophysiological properties
of large cell populations as an *in vitro* reference for cell networks *in vivo*.

Introduction

The brain is a fascinating and amazing organ in the human body. Functionally, it is able to process all of the information received from sensory organs into information like vision, hearing, balance, smell and taste. Moreover, it regulates many bodily functions in an unconscious manner, like e.g. body temperature, blood pressure, breathing, gastrointestinal functions and so on. Therefore, the brain can be considered as the most complex organ forming the 'central processing unit' within humans and vertebrates.

Since the beginning of the modern medicine, especially in neuroscience, the investigation and understanding of the brain functions was of major interest. Much effort has been made and many studies in this field were carried out to obtain profound knowledge related to brain processes. A major aspect of the brain functionality is the *communication* between brain cells, that are organized in highly complex networks. This collaborative activity of thousands of brain cells is considered to include the complex brain functions like sensation and cognition. In contrast, many people suffer from neurodegenerative brain diseases like Alzheimer's or Parkinson's disease, loss of memory or postoperative cognitive dysfunction. Such diseases effect the brain morphology, but also the communication within neuronal networks and lead to pronounced symptoms like for example shivering, confusion and dementia, which strongly decrease the health-related quality of life of the affected patients.

For the improvement of the understanding of some of these complex processes in the brain, the objective of this work was the study of *brain cell communication*. Since brain cells, in particular neurons, communicate by means of ionic currents in general, we focused on the monitoring of their bioelectronic activity. For this purpose, low-frequency electric current measurements within multicellular brain cell populations *in vitro* were performed.

In the current work, we investigated the bioelectronic activity in large cell populations. Therefore we developed new sensing devices that unambiguously allow the non-invasive measuring of ionic current fluctuations within cell networks, sensitive in the femtoampere range. For such ultra sensitive current measurements, we established a suitable experimental setup, that allows not only precise and reproducible measurements, but also the recording of bioelectronic activity of cell populations *in vitro* over a long time. Therefore, we developed a data acquisition software in LabVIEW. For further analysis, quantification and comparison of the obtained cur-

rent signals, we developed a MATLAB software for spectral analysis.

With our state-of-the-art setup, we were able to study the bioelectronic activity of cultured glioma cell populations, which originate from brain tumor. In these experiments, we investigated the origins of the bioelectronic signals detected with our setup. These current fluctuations, which we termed current noise, were found to be related to potassium and sodium ion channels within the cell membrane. Thus, we offer here a unique approach for studying electrophysiological properties of large cancer cell populations as an *in vitro* reference for tumor bulks *in vivo*.

Lastly, we performed the long-term monitoring of bioelectronic activity in primary, embryonic neuron populations from the hippocampus in the murine brain. Here, we observed the formation of neuronal networks *in vitro* on our transducers, that reveal insights in the neuronal network communication. In-depth studies on the neuronal network behavior and communication will help to understand and maybe treat brain diseases in the future.

In this work, we present our approach to investigate brain cell communication with the following outline: In the first chapter, we illustrate general biological and bioelectronic processes of brain cells. We identify noise sources within the cells, which we relate to fundamental knowledge of noise, and present the method of spectral analysis. After a brief overview of existing bioelectronic devices, we explain the basics of microelectrode theory which includes an equivalent circuit model of our transducer. In the second chapter, the in-house fabrication of newly developed transducers is depicted. Chapter 3 describes the experimental setup used for bioelectronic measurements, which includes aspects and parameters of low noise current recordings. The results of bioelectronic measurements are shown in chapter 4. Here, we present detection limit of our system and the results of experiments with glioma cells, including the identification of the obtained current noise signals, which has also been published during this work [1]. Moreover, the evolution of bioelectronic activity in a maturing neuronal network is shown.

1 Fundamentals

In this section, we firstly present an overview of biological basics related to brain cells, that include morphological and physiological aspects. The process of cell metabolism and neuronal electric signaling is based on ionic currents, why we introduce the *bioelectronic activity* of brain cells. The ionic currents related to cells, and in particular ion channels in the cell membrane, are considered to be current noise sources. Current noise can supplementary be described in a frequency representation, the so called current noise spectrum. After a general introduction to the concept of thermal noise, we depict the method for obtaining the current noise spectrum of a current signal. We then identify different noise sources in the cell membrane and discuss their expected spectral behavior prior to explaining the spectral estimation of such current noise signals in MATLAB.

A general overview of existing devices for different bioelectronic measurements is given. Finally, we discuss several aspects concerning the microelectrode theory, which includes fundamental knowledge on the interface of electrodes with aqueous electrolytes. We end this chapter by presenting our approach to model the electric properties of this interface by means of a modified Double RC equivalent circuit model.

1.1 Bioelectronic activity of brain cells

The brain is the most important organ of the nervous system in vertebrates. The main cell classes in the nervous tissue of the brain are essentially neurons and glial cells or glia. Neurons are electrically excitable cells, which are able to receive, process and transmit information through electrical and chemical signals. Therefore, neurons can be considered to be the signaling units of the nervous system [2]. Glia cells surround the neurons. They can be divided in three major types: Oligodendrocytes and Schwann cells, which envelop and electrically insulate the neurons and astrocytes, which play a major role in the neuronal nutrition cycle. Glia cells are less electrically excitable and therefore not directly involved in the electric signaling process like neurons. The glia cells support the neurons in their signaling duty.

Neurons are specialized cells for a particular purpose or application. There exist around 100 distinct types of neurons like retinal neurons, hippocampal neurons, motor neurons etc. They show huge variances in their morphology and functional behavior. Neurons interconnect with each other and form highly complex and functionalized networks within the brain and the nervous system.

Fig. 1.1 shows a basic illustration of a neuron. Neurons basically consist of a cell body, the soma, and two different types of cellular extensions: axons and dendrites. The axons are able to forward electrical signals from the neuron to a following cell, while the dendrites receive signals from other cells.

Neurons typically communicate via synapses. At these inter-neuronal connections, an axon connects to a dendrite of another cell. Here, an electric signal is translated into a chemical signal: Inside the synapse, the synaptic cleft, signaling molecules, the neurotransmitters, are released from the pre-synaptic neuron (axon). These neurotransmitters diffuse towards the receiving, post-synaptic neuron (dendrite), where the chemical signal is re-translated into an electrical signal. In this manner, neuronal signals are transmitted along a neuronal network. *In vivo* and *in vitro* experiments on neuronal cells use electrical stimulation to provoke the release of neurotransmitters, and therefore electrically excite the cells under test.
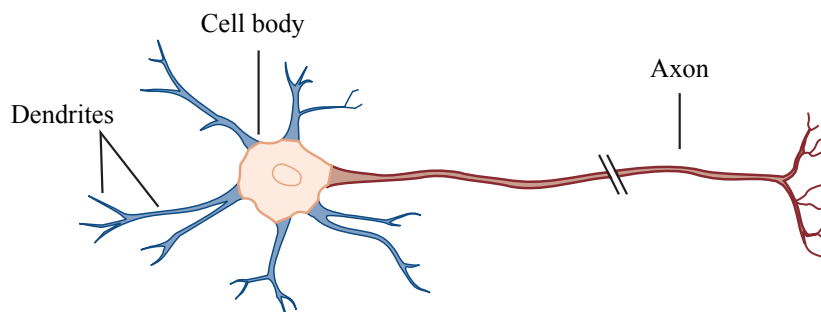

Figure 1.1: Schematic representation of a basic neuron with the cell body and cellular extensions, the axons, which forward electric signals to a following cell and the dendrites, that receive signals from other cells [2].

Like all cells in the human body, a neuron is enclosed by a cell membrane, which confines the cell from the surrounding environment. This surrounding environment is called the *extracellular* space or matrix.

A schematic representation of the cell membrane structure is shown in fig. 1.2. The cell membrane is a bilayer structure of lipid molecules, which embeds a large variety of functional membrane proteins. Among these proteins, there are many specific ion channels existing in a cell membrane. The ion channels allow electrically charged ions, to selectively move across the cell membrane along a chemical concentration gradient. In neurons, ion channels for potassium (K^+) and sodium (Na^+) ions play a major role for neuronal signaling.

Moreover, there exist metabolic processes in the cell membrane, called ion pumps. They are able to regulate the cell's metabolism by active transport of ions through the cell membrane. One of the most important ion pumps in neurons is the so called *sodium-potassium pump*, which facilitates continuous transport of potassium ions inside the cell, while sodium ions are exported into the extracellular medium. Due to the resulting different ionic concentrations inside and outside the cell, neurons are able to build up a resting membrane potential. The chemical concentration gradient leads to a measurable voltage difference compared to the extracellular medium of about $-70\,\mathrm{mV}$, see fig. 1.2.

Summarizing, the ion pumps within cell membranes build up a resting state of the cell membrane. which exhibits a membrane potential in neurons. The ion channels are able to open in a functional manner, and therefore facilitate fast transport of a huge amount of ions through the cell membrane [3].
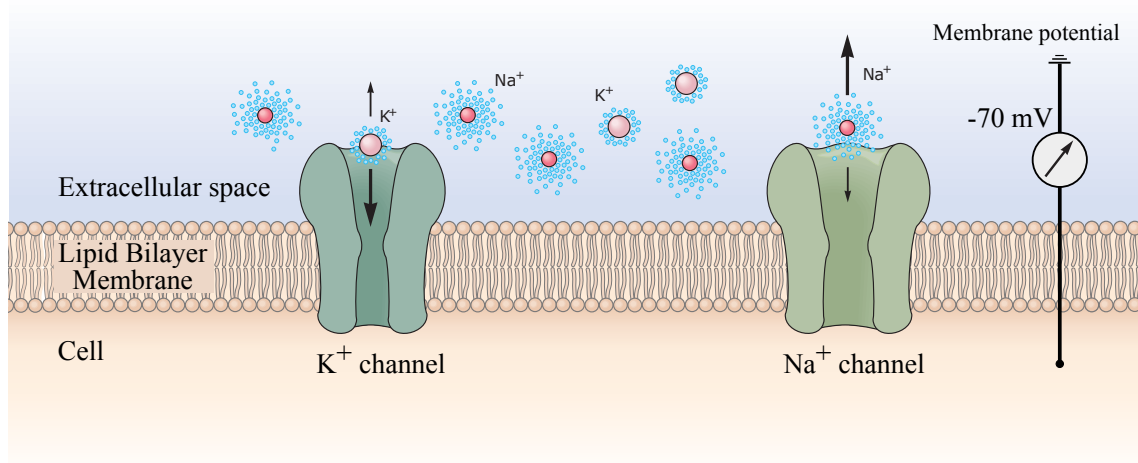
Figure 1.2: Schematic representation of the cell membrane, which borders the cell's interior from the extracellular space. The cell membrane, a lipid bilayer structure, incorporates specific ion channels, that are able to change their ionic permeability and thus allow specific ions to move across the cell membrane. Differences in ion concentration inside and outside a neuron generate a resting membrane potential, which is around $-70\,\mathrm{mV}$ [2].

In neurons, the permeability for ions of the bilayer membrane can be changed by external electric or chemical stimuli. This means that particular ion channels change from insulating to conductive properties for a particular ion and vice versa. By an incoming appropriate stimulus, the voltage gated sodium channels open followed by a fast influx of sodium ions inside the cell. The resulting charge inside the cell changes from negative to positive, which is known as depolarization. Shortly after, the positive charge inside the cell leads to closing of the sodium channels and opening of the voltage-gated potassium channels, resulting in a blow-out of potassium ions which move down the electrochemical gradient into the extra-cellular matrix. This is known as repolarization. The sodium-potassium pump then restores the resting state as before. This behavior can be electrically measured and is called action potential. A typical time course of the membrane voltage during an action potential is shown in fig. 1.3. The action potential can be forwarded to another connected cell via the conducting axon of the neuron. Therefore, this mechanism is able to transmit information in neuronal networks.

The axons and synapses of neurons are surrounded by glia cells. These glia cells modulate the rate of signal propagation and synaptic action by also controlling the uptake of neurotransmitters. Hence, they have a major role in regulating the neuron's metabolic functions and support the neuronal signal transmission
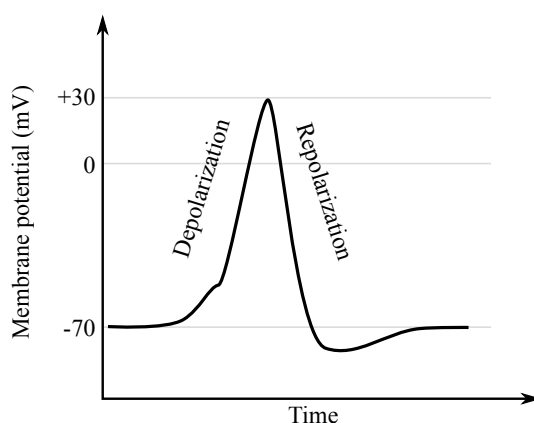
Figure 1.3: Schematic representation of an action potential from a neuron. The characteristic time course of the membrane potential is determined by firstly a fast influx of sodium ions (Depolarization) followed by a blow-out of potassium ions (Repolarization). This process represents the basic mechanism of neuronal signaling.

Glia cells, Greek for *glue*, surround the cell bodies, axons and dendrites of neurons and therefore stabilize the brain tissue. They differ from neurons in morphology, as they do not form axons or dendrites. Moreover, the membrane properties of glia cells are different from neurons. They feature different functionality. Some glia cells, the oligodendrocytes, insulate the axons of the neurons from their environment. Other

glia cells, like astrocytes, are located close to the synapse. They regulate different processes within or close to the synapses, like the concentration of K^+ ions and release of growth factors. They perform different other tasks of 'housekeeping' and therefore support the proper neuronal signaling. In the brain of vertebrates, there exist around 2 to 10 times more glia cells than neurons. The glia cells are of major importance for neurons in the nervous system. However, the function of glia cells is not fully clear [2].

A prevalent disease is the glioma, which is a brain tumor that arises from glia cells. The C6 glioma cell line is one of the most intensely studied cell lines within glioma cells, as they are suitable to study properties of glia cells [4]. C6 glioma cells multiply with time, as they are cancer cells.

The mechanisms described previously in a very simplified way are the basic elements of neuronal signaling. Ionic currents through the cell membrane lead to a measurable membrane potential. The membrane potential of neurons can be modified due to appropriate stimuli, which can result in events of electric activity like action potentials. The action potentials happen within milliseconds and are of complex nature, as the transmitted biological information is encoded within patterns of pulse trains and not obvious to understand.

Summarizing, the processes related to cells like ionic currents, the membrane potential, action potentials and so on are important biological events inside the brain. These processes operate based on electric activity, why they are considered as *bioelectronic activity* of brain cells.

In this work, experiments were performed with cultured rat C6 glioma cells and murine primary, embryonic hippocampal neurons. The investigation of bioelectronic activity within these different types of brain cells is the objective of this work.

1.2 Spectral analysis of bioelectronic signals

For the investigation of bioelectronic signals obtained from cell populations, we consider the cell membrane to be a noise generator. Here, we introduce the concept of thermal noise, which is related to resistors. Afterwards, the mathematical method for spectral estimation is presented. After identification of different noise sources in the cell membrane, we use a current signal from C6 glioma cells to exemplify the software for estimation of the power spectral density in MATLAB.

1.2.1 Thermal noise

At the end of an ohmic resistor with no bias applied, there is always a small fluctuating voltage detectable. This phenomenon of voltage noise was first measured and explained by Johnson and Nyquist [5]. This noise voltage V_n is due to the Brownian motion of the charge carriers. The charge carriers, in this case electrons, move freely inside the conducting resistor in random directions. The electron velocity depends on the absolute temperature T. The motion of the electrons, which all hold the elementary charge e^-, is an electric current. This random current, or noise current I_n, is minute but not zero. Following Ohm's law, the noise voltage and the noise current can be correlated as

$$V_n = I_n \cdot R, \tag{1.1}$$

where R is the resistance. The so called Johnson-Nyquist voltage noise in a frequency window of df can be expressed by the average squared voltage

$$\langle V_n^2 \rangle = 4 \, k_b \, T \, R \, df \quad , \tag{1.2}$$

where k_b is the Boltzmann's constant ($1.38 \cdot 10^{-23} \, \text{J/K}$), T is the temperature in Kelvin, R is the resistance in Ohms and df is the bandwidth of the measurement in Hz. According to eq. (1.1), the average squared current noise can therefore be stated in analogy to eq.(1.2) as

$$\langle I_n^2 \rangle = \frac{4 \, k_b \, T \, df}{R}. \tag{1.3}$$

This thermal noise in voltage and current can be expressed in the frequency domain, where the average square voltage and the average square current in a frequency band df are

$$\frac{V_n^2}{df} = 4 \, k_b \, T \, R \qquad \text{and} \qquad \frac{I_n^2}{df} = \frac{4 \, k_b \, T}{R}. \tag{1.4}$$

These identities state that the so called *voltage power spectral density* and *current power spectral density* respectively, which will be discussed in detail in the next section, are constant for each frequency interval df in the spectral representation. The shape of the thermal noise spectrum is therefore a flat, constant curve and is termed *white noise*. Fig. 1.4 represents the calculated power spectral density functions for voltage and current noise for an ohmic resistor of 800 Ohm at 300 K. The voltage noise is represented in black, the current noise in red.
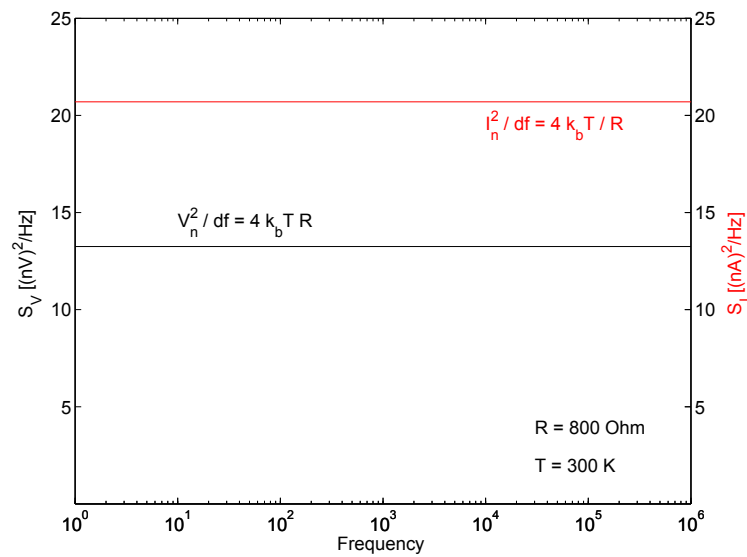

Figure 1.4: Calculated power spectral density function for voltage noise (black) and current noise (red) of an ohmic resistor of 800 Ohm at 300 K. As the origin of the resistor noise is thermal noise, the spectra show a flat curve. This is termed white noise.

1.2.2 Current noise spectrum S_I

The goal of spectral analysis or *spectral estimation* is to obtain information about the spectral distribution of a discrete signal. The spectral representation is a supplementary expression of a set of data, in addition to the basic time course representation of the magnitude. This is useful for the quantification and comparison of the cell's bioelectronic activity in the frequency range. The spectral analysis reveals the spectral composition of a signal and helps to detect specific signals that are buried in the overall signal noise.

For post-processing data analysis in the frequency range, we calculate the *power spectral density* (PSD) of a recorded, discrete current signal with MATLAB. The developed software is presented in section 1.2.4. The method we use to estimate the PSD is described in this section.

In signal theory, the total energy E_s of a continuous signal $x(t)$ can be described as

$$E_s = \int_{-\infty}^{+\infty} |x(t)|^2 \, \mathrm{d}t. \tag{1.5}$$

If we consider a finite set of data, the average power $\overline{P}$ is then given by

$$\overline{P} = \lim_{T \to \infty} \frac{1}{T} \int_0^{+T} |x(t)|^2 \, \mathrm{d}t, \tag{1.6}$$

which is similar to the definition of the autocorrelation function

$$R_{xx}(\tau) = \lim_{T \to \infty} \frac{1}{T} \int_0^{+T} x(t) \cdot x(t + \tau) \, \mathrm{d}t, \tag{1.7}$$

where a function $x(t)$ is multiplied by itself, but with a shift determined by the time lag τ. If we consider τ to be zero, we obtain

$$R_{xx}(0) = \lim_{T \to \infty} \frac{1}{T} \int_0^{+T} x(t) \cdot x(t) \, \mathrm{d}t, \tag{1.8}$$

which equals eq.(1.6). According to *Wiener-Chintschin's theorem* [6], the power spectral density function S_{xx} of a stationary signal is the Fourier transform of its corresponding autocorrelation function (eq. 1.7), which, for each particular frequency f, then is

$$S_{xx}(f) = \frac{1}{\sqrt{2\pi}} \int_{-\infty}^{\infty} R_{xx}(\tau) \cdot e^{-j\,2\pi f \cdot \tau} \, \mathrm{d}\tau. \tag{1.9}$$

Considering a current signal $x(t) = I(t)$, we therefore obtain the current noise spectrum $S_I(f)$, with units in

$$[S_I(f)] = \frac{A^2}{Hz}. \tag{1.10}$$

The representation in a current spectrum plot shows the calculated function of *power spectral density* $S_I(f)$ of the current $I(t)$ over the frequency f.

1.2.3 Current noise in a cell membrane

In section 1.1 we considered the origin of bioelectronic activity of cells to be ionic currents across the cell membrane, see fig. 1.2. These minute current oscillations, which we termed *membrane current noise*, are usually ascribed to fluctuations of the membrane potential in individual cells, since the membrane potential of living cells is never entirely constant, but subject to slight fluctuations due to their constant physiological activities. Such oscillations in membrane potential are caused by bidirectional flow of Na^+ and K^+ ions [1].

Assuming a resting state of the cell membrane, meaning an equilibrium between influx and efflux of ions due to the continuous activity of ion pumps and ion channels described in 1.1, the cell membrane is very resistive and can be conceived as a resistor [3]. Therefore, especially the ion pumps in the cell membrane are considered to be a source of thermal noise. When a biological process occurs like for example a membrane depolarization within an action potential in a neuron, or other bioelectronic activity as observed in glia cells [1], the resting state of the cell membrane is strongly disturbed. This behavior can not be simply described by a resistor, as it deviates from equilibrium conditions.

Therefore, we consider these voltage fluctuations and current fluctuations respectively of a cell membrane to be composed of two main components, which we illustrate in fig. 1.5. Firstly, some of these fluctuations happen continuously within the cell's metabolism, which we associate with thermal current noise due to a resting state of the cell membrane, which is related to the ion pumps. Secondly, some fast biological events concerning the ion channels do have a functional character, like e.g. fast ion transport during action potentials, which is expected to show a different spectral behavior, compared to thermal noise. The current noise spectrum S_I is expected to be proportional to $1/f^\gamma$, where in most cases $1.5 \leq \gamma \leq 2$. The occurring processes related to ion channels are considered to be relatively low-frequent and exceed the thermal noise in a cell membrane of a factor about 1000 [3].

The biological processes relating to the cell membranes are highly complex. However, for a basic understanding, the very simplified description of the cell membrane being a resistor is sufficient.
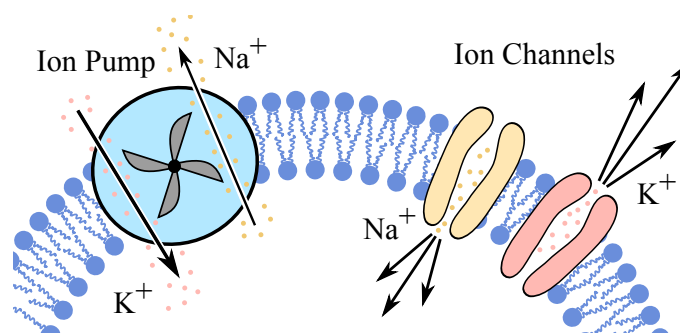

Figure 1.5: Schematic representation of noise sources in the cell membrane. Thermal noise is associated with the resting state of the cell membrane, which relates to ion pumps. Functional events like action potentials, that include fast ion flux through ion channels, are much higher in noise magnitude.

1.2.4 Spectral analysis algorithm in MATLAB

For the investigation of membrane current noise, we analyze the recorded current signals of the cell populations by means of the current noise spectrum, which we discussed in the previous section. Therefore we developed a software in MATLAB, that features the spectral analysis, moving average filtering and downsampling of the spectra. In the following, we discuss different aspects of the used algorithms and present the current noise spectrum obtained from a current measurement of C6 glioma cells. For the following examples, we deliberately chose a signal, where the cells seemed to be in a 'quiescent' state s to emphasize the spectral behavior, which can be related to thermal noise in the cell membranes described in the previous section. The employed experimental setup for current measurements of cell populations is presented in chapter 3.

In MATLAB, the easiest way to obtain the *power spectral density* (PSD) of a current signal is the use of the `periodogram` algorithm:

```
[SI F] = periodogram(current,flattopwin(nfft),nfft, fs, ...
    'psd');
```

, where `current` contains the signal, `flattopwin(nfft)` defines a *flattop* windowing function of the length `nfft`, which is the number of samples used for calculation, and `fs` is the sampling rate. It returns a matrix which contains the values of the PSD function `SI` and the according frequencies `F`, according to section 1.2.2.

For the estimation of `SI`, this algorithm first multiplies the signal with a flattop window of equal length to avoid artifacts due to finite signal length. It then calculates the autocorrelation function of the windowed signal and afterwards executes the Fourier transform.

In fig. 1.6a, we show the obtained current spectrum by using `periodogram`. The value of the current PSD function $S_I(f)$ is shown over the frequency range. The time course of the analyzed current signal from C6 glioma cells is represented in fig. 1.6b. It is obvious that this spectrum very noisy, especially within the higher frequencies. As mentioned before, the spectrum shows a relatively flat slope as expected, which we correlate to a rather resistive behavior of the cell membranes, which typically exhibits white noise character.
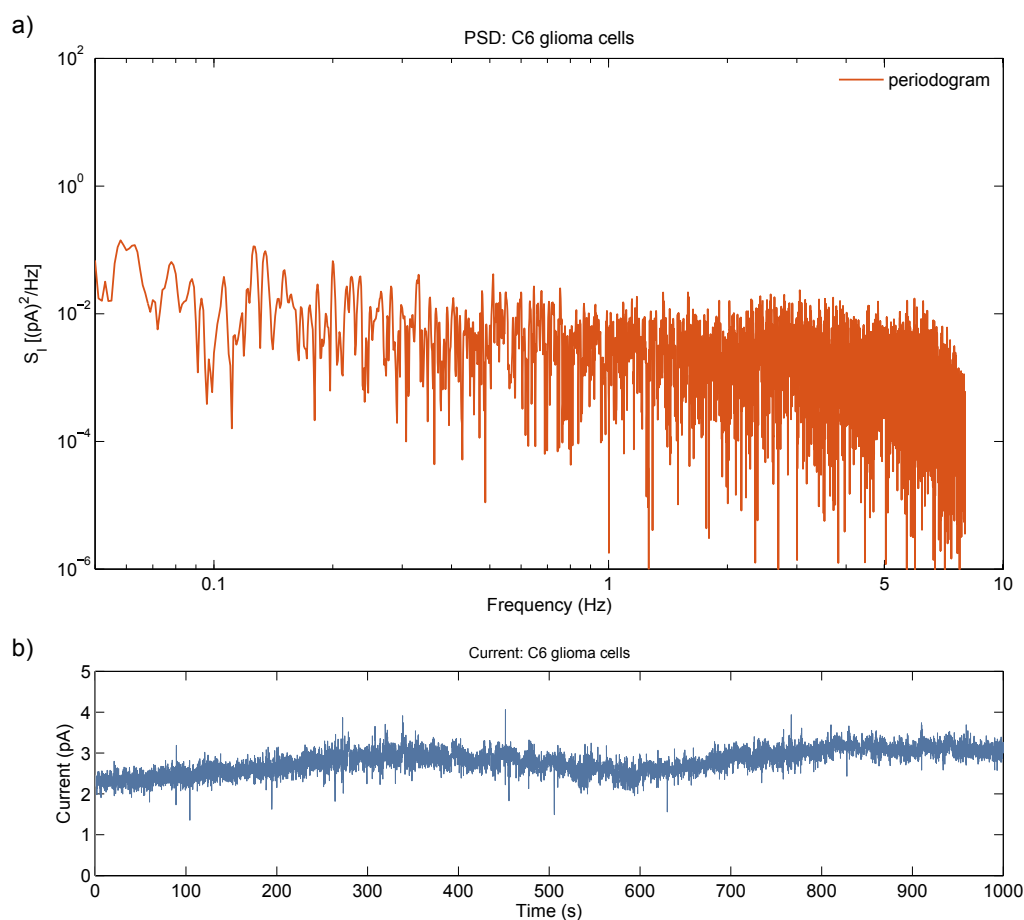
Figure 1.6: a) Current noise spectrum of the C6 glioma current signal shown in b) obtained with periodogram in MATLAB. The spectrum shows a high amount of fluctuations.

As the high amount of spectral noise is inconvenient for further data analysis, the MATLAB analysing software was improved by using the `pwelch` algorithm for PSD estimation. This method is based on the `periodogram` algorithm, but holds averaging features and more control of the estimation parameters:

```
[SI F] = pwelch(current,flattopwin(win_pwelch), ...
      over_pwelch, nfft_pwelch,fs); .
```

The `pwelch` algorithm firstly divides the input signal into segments with length `win_pwelch` and multiplies each segment with a flattop window. The segments

overlap according to the number of samples specified in `over_pwelch`, which was typically 50 samples. The PSD for each segment is calculated separately and these multiple PSD plots are then averaged. Fig. 1.7a shows the PSD analysis of the same signal obtained with `pwelch`. In this examples, the current signal was divided in 4 segments, which are shown in fig. 1.7b. For data analysis and comparison, the `pwelch` algorithm is much more convenient, because the PSD curves are smoother compared to `periodogram`. However, one has to be aware that the averaging parameters do effect the result of the obtained PSD.
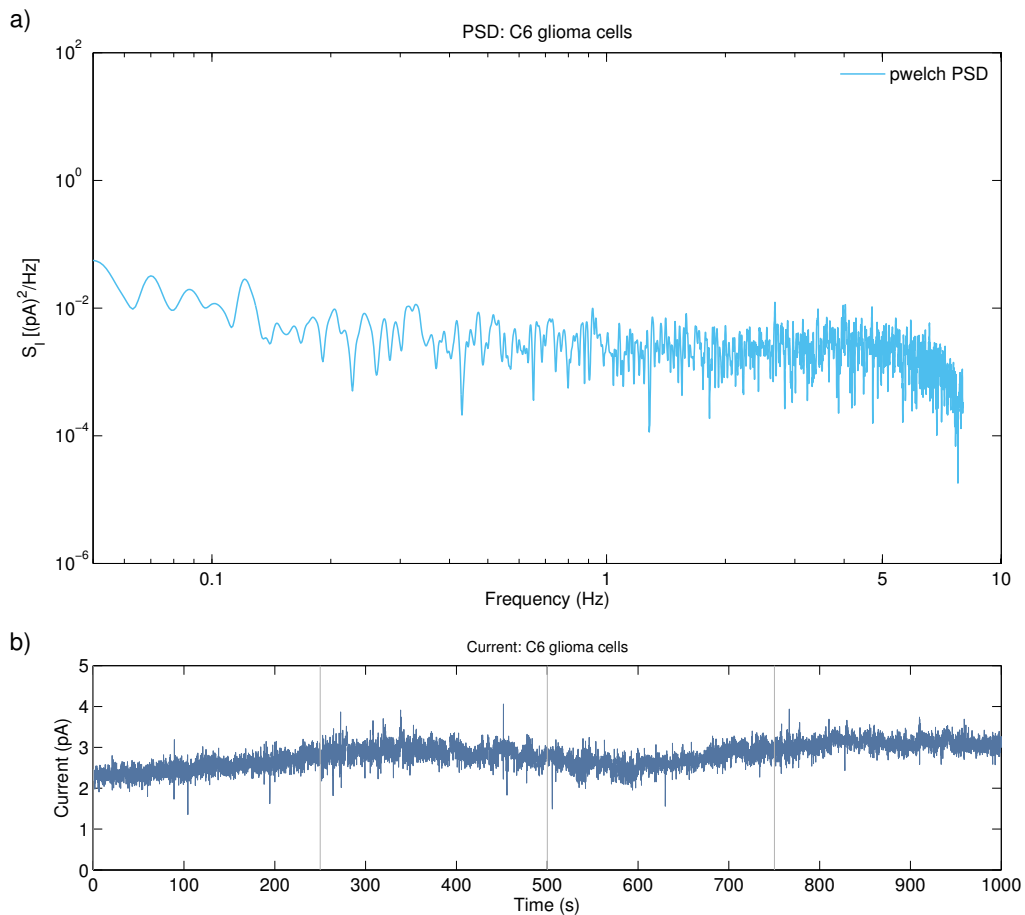

Figure 1.7: a) Current noise spectrum of the same C6 glioma current signal shown in b) obtained with pwelch algorithm in MATLAB. The spectrum is smoothed due to averaging of the pwelch algorithm, which divides the signal in several windows, shown in b)

Another method for smoothing the PSD plot in post-processing is the centered *moving average* (MAV) filtering. For a fixed time t_0 (one sample), this filter generates a new value $y_{MAV}(t_0)$ for this sample by calculation of the arithmetic mean of n neighboring samples. It can be described as

$$y_{MAV}(t_0) \; = \; \frac{1}{n} \sum_{i=-\frac{n-1}{2}}^{\frac{n-1}{2}} y(t+i) \quad ; \quad n = 3, 5, 7, ... \tag{1.11}$$

. As this filter smoothes a signal, it acts like a low-pass filter, why it has to be used carefully. By filtering the PSD plots, a certain amount of spectral information will be lost inevitably. Again, setting the parameter for the MAV is a trade-off between smoothing and loss of information.

Moreover, the huge amount of data contained in one PSD plot can be further reduced by downsampling the data. In terms of data handling and visualization, it is favourable to reduce the amount of samples in a PSD when considering a limited computer performance. The downsampling will be advantageous especially for the method of *spectrogram*, which will be described later.

In a N-fold downsampling, every Nth sample of the dataset will be kept, while all others are erased. The result of the *moving average* filtering and the *downsampling* are shown in fig. 1.8a, which was again obtained from the same current signal shown in fig. 1.7b. In this example, the number of comprised samples for the MAV filter was $n = 25$. This results in a significant smoothing of the spectrum, represented by the dark blue curve. The MAV was followed by 40-fold downsampling, which is displayed by the yellow curve.

Fig. 1.8b shows a magnification of the plot in fig. 1.8a to illustrate the effects of the available methods for post-processing data modification and analysis in detail. It becomes apparent, that the use of filtering and downsampling leads to both noise and data reduction, but also comes with a certain loss of information.

In this work, the order of post-processing the data was firstly the MAV filter and afterwards the downsampling for all analyses. Simulations on this issue have shown an enormously increased loss of spectral information when performing downsampling prior to MAV filtering (not shown).

The current noise spectrum of the C6 glioma cells presented in fig. 1.8a shows a flattened, almost plane slope in the frequency range above roughly 1 Hz. However, the spectrum is not completely flat but contains small spectral fluctuations in the range of 10^{-2} (pA)^2/Hz. This region of the spectrum can be correlated to a thermal noise contribution of the cell's membrane current noise as mentioned in section 1.2.1. In the low frequency range below 1 Hz, the noise spectrum deviates from the ideal thermal noise behavior. The spectrum rises to higher values, that correlate with biologically relevant processes like ionic currents through Na$^+$ and K$^+$ ion channels [1]. The spectra of such bioelectronic activity of cells, which originates

from ion channels, outstand from the random membrane fluctuations associated with thermal noise. Bioelectronic activity within glioma cells and neurons can be significantly detected by means of spectral analysis. Therefore, the PSD analysis is a suitable tool for the investigation of bioelectronic activity of cells.

The analyzed signal of C6 glioma cells is an example of recorded current signals. In this case, the cells show a relatively low electric activity, as living cells perform different states of bioelectronic activity from time to time. This is usual, as a population of cells is a biological system that is never entirely constant. In [1] and section 4.2, we show current signals obtained from C6 glioma cells with different bioelectronic activity.
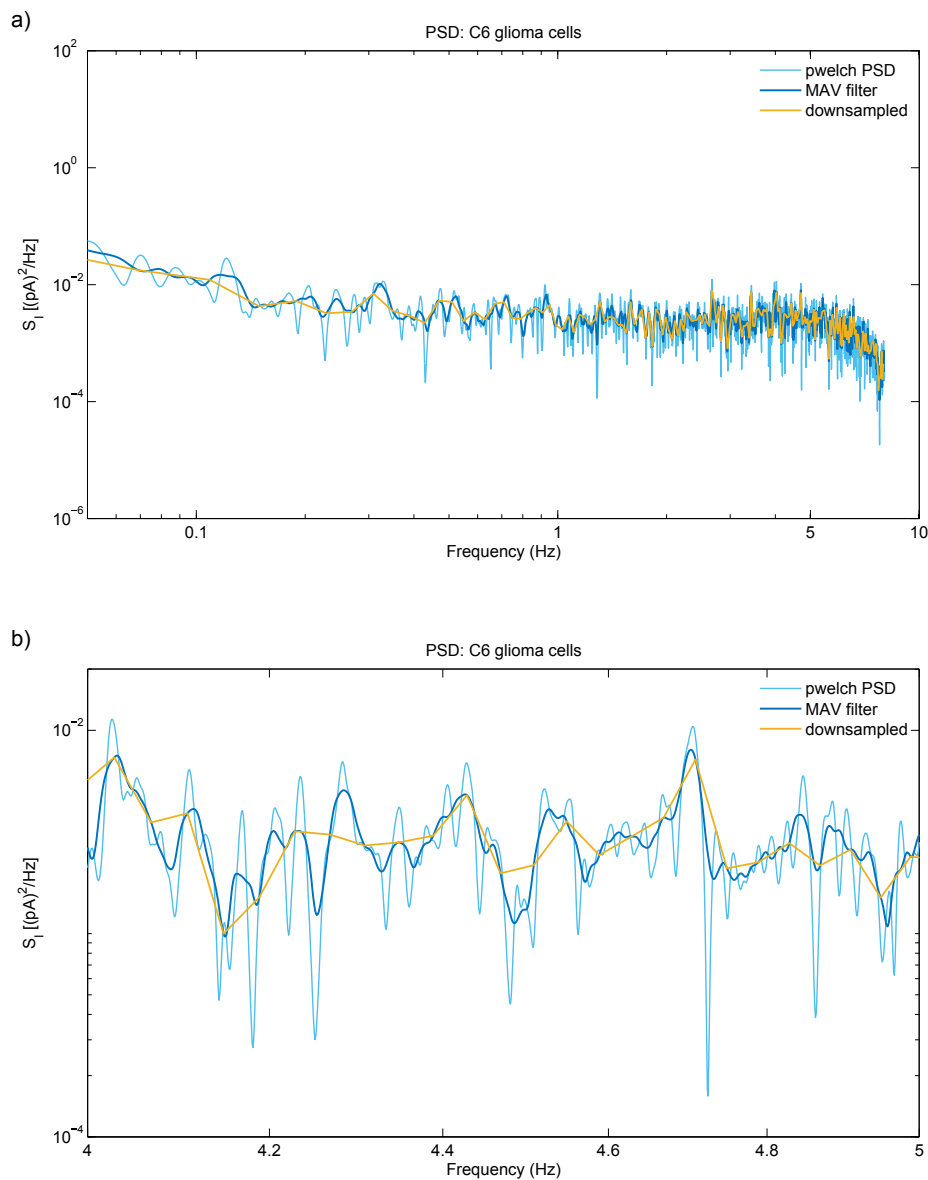

Figure 1.8: MAVDS

1.3 Bioelectronic devices for cell monitoring

A biosensor is a device, which combines biological components with a physico-chemical transducer. Such a device is able to detect or analyze analytes like molecules or ions inside a biological sample, or changes of physical measures due to certain biological properties.

Among a huge variety of existing biosensing devices, one of the most prominent biosensor family are the cell-based biosensors. Cell-based biosensors are able to acquire biologically relevant information directly from living cells and are used in different fields like pharmaceutical effect analysis, monitoring of cell growth or cellular physiological parameter detection. Cell-based biosensors are suitable for *in situ*, *in vivo* and *in vitro* monitoring of cells and offer a broad spectrum of detection capabilities [7].

In this section, we give an overview of existing biosensors, that deal with *electronic* processes related to cells. We therefore consider these devices as *bioelectronic* transducers, which are able to detect particular electrical properties of single cells or cell populations due to their physiological activity.

For the investigation of cell adhesion, proliferation, growth and migration in real time, electrical cell-substrate impedance sensors (ECIS) are widely used. Here, microelectrodes are fabricated on the surface of a sensor, for example a glass or silicon substrate. Cells attach to the sensor surface and thus cover the transducing electrodes. For impedance spectroscopy, either an ac current is applied to the electrodes and the voltage is measured with respect to amplitude and phase shift, or vice versa, where an ac voltage is applied and the current is measured accordingly. The result is the impedance as a function of applied frequency $Z(f)$, which can be widely influenced by the cells in terms of for example metabolic processes, membrane properties and adhesion behavior.

Another approach to study cells or cell populations makes use of the field effect transistor (FET). This method is based on the idea, that cells are placed on top of a FET structure instead of a metallic gate. With electrically active or excitable cells like muscle cells or neurons acting as a gate for the transistor, it is relatively easy to record such bioelectronic processes, as they are able to directly change the electric field inside the transistor. Moreover, cell metabolism parameters include for example the change of the extracellular pH value, oxygen consumption, carbon dioxide production and ion concentration. These parameters effect different electric properties of the extracellular matrix, like for example conductivity. With such a FET structure, these changes can be detected, while the cells and the extracellular matrix act as a gate for the transistor. Hence, this type of transducers is also suitable to study particular properties of electrically inactive cells and cell populations.

A modification of the FET approach is the coating of a FET structure with a conductive organic polymer like PEDOT[1] as a gate. One advantage of these uprising organic field effect transistor (OFETs) can be found in the electric properties of such organic materials, as for example PEDOT exhibits both electronic and ionic conductivity. The cells, which cover the polymer gate, release ions which can easily travel through the polymer layer towards the detection system. Moreover, organic polymers offer a wide range of advantages in terms of chemical modification, soft mechanic properties, good biocompatibility and interface properties, like oxide-free interfaces with aqueous electrolytes, why they are quiet promising for bioelectronics [8].

To study particular regions of a cell membrane, the patch-clamp technique is an established method and represents a powerful tool for investigation of single or multiple ion channels of *single* cells. Here, a fire-polished glass micropipet, with open tip diameter of about 1 μm is used to probe a small cell membrane patch. The glass pipet forms a seal resistance with the cell membrane that is in the range of gigaohms, which is the most important feature of this technique. Hence, the ionic current of very few ion channel can be detected and recorded. With the patch-clamp technique, many different aspects of cell membranes, that correspond to ion channels, can be investigated, like ion channel research in general and drug screening, which is related to the behavior of specific receptors under different chemical agents. Based on the idea of conventional patch-clamping, planar patch clamp chips have been developed and used, that feature different materials and pursue the further improvement of this method.

In contrast to the patch-clamp technique, which can only measure single spots of the cell membrane, the substrate-integrated microelectrode arrays (MEA) have become a state-of-the-art tool for investigation of whole cells, particularly neurons, in neuroscience. A MEA basically consists of a substrate with multiple spatially distributed electrodes, and peripheral detection system including amplifiers and data analysis. There exist numerous designs of electrode array transducers, according to the particular purpose. Some MEAs can be used for studies on samples of whole tissue. Neurons, or other cells, are either placed on these microelectrode arrays with high precision micromanipulators, or cell populations are grown in the transducer *in vitro*. Hence, a neuron, with its cellular extensions, is able to cover several single electrodes. The electrodes are usually made of gold, but also different electrode materials evolve. Each electrode can either be used for measuring the electrical activity or electrical stimulation of the cell in a limited region. Therefore, the spatio-temporal response of neurons to different stimuli can be investigated in a wide range, including the effects of chemical agents or other influencing parame-

---

[1]Poly-3,4-ethylendioxythiophen

ters. Additionally, one or more electrodes can be used for local current stimulation of different cell regions while measuring the electric responses of different regions of the cell. A typical MEA transducer and a microelectrode array is shown in fig. 1.9. One of the first MEAs was reported in 1974 [9]. In modern MEA systems, usually the voltage of each electrode is measured by differential amplifiers or with FET [10]. The method is based on direct ohmic coupling of the electrode with the extracellular medium or the cell respectively. Hence, the resolution is in the range of milli- or microvolts. There exist MEA systems, that measure current with a detectability in the milli- or microampere range. Hence, they are fully applicable for neuronal studies due to the relatively high electrical activity of for example neural extracellular action potentials in the range of several millivolts. Since MEA systems are restricted by these voltage and current limits, it is difficult to study electrically 'quiescent' cells, that do not feature pronounced electrical excitability.
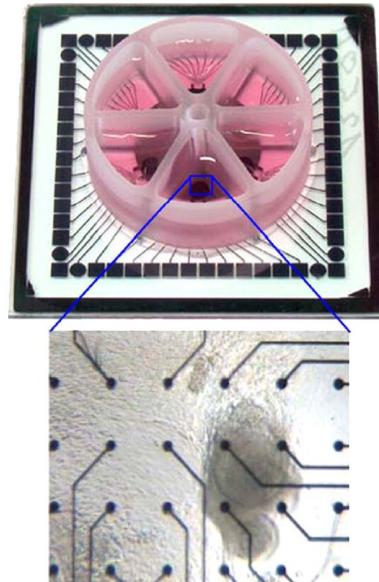

Figure 1.9: Typical MEA transducer for *in vitro* multichannel recordings of cells. This transducer features 6 different wells. The electrode array structure is magnified [7].

Our developed system for low-noise current recordings in the picoampere range, which is presented in this work, follows the idea of recording of cell populations *in vitro* with transducers, that feature gold electrodes in contact with the culture medium and the cells. The electrical detection method in our system is based on the capacitive coupling of 'device under test', meaning the cells in the culture medium, and the *blocking* electrodes. Therefore, we cover the transducers and the electrodes with an organic insulator. To this end we use poly-L-lysine as it can be used at the

same time as an adhesion promoter for cells.

1.4 Microelectrode theory

Our sensing system is based on gold electrodes in contact with the culture medium and the cells. Similar to MEA systems, we here introduce the theory of such micro-electrodes.

The investigation of bioelectronic activity of cell populations *in vitro* requires a measuring system that is able to detect the bio-signals of interest accurately.
The cells release ions, which move in the culture medium, and therefore represent *ionic* currents and hence generate potential differences. On the opposite, the peripheral measuring equipment like cables, amplifiers etc. is made of many metallic components that can only deal with *electronic* conductance. This implies the necessity of a transducer, which is able to transfer the ionic bio-signals of the cells into a measurable electronic signal within the experimental equipment.

For this purpose, cell populations will be cultivated on our transducers, that feature thin gold microelectrodes on glass substrates. For proper maintenance of cells, it is crucial to provide the cells with nutrient solution (culture medium), that contains ideal nutrient matter for the particular cells. The culture medium is basically a solution of high salinity, that contains different chemical substances and particularly solvated ions, and is therefore considered as electrolyte.
The configuration of gold electrodes immersed in culture medium leads to the model of a *metal-electrolyte interface* at the junction site. The physical processes at this interface incorporate the method for detection of the bio-signals and it is therefore essential to study the interface behavior in detail.

In the following sections, we will discuss the physico-chemical processes at the metal-electrolyte interface and present our approach to model the electronic behavior by means of a modified equivalent circuit.

1.4.1 The metal – electrolyte interface

When a metallic electrode is immersed into ionic conducting solution, or electrolyte, the charge carriers near the interface get affected alternately, which will be described in this section.

The charge carriers within the metallic electrode are solely electrons, which are able to move freely inside the metal, known as electronic conductivity. In a spatially limited region of the metal surface, an equilibrium will be established where the permanent inflow and outflow of electrons to and from the metal will be equal. This results in a net current of zero [7].

Fig. 1.10 illustrates the metal-electrolyte interface in a schematic representation. The electrons are mostly localized at the surface of the metal. At zero bias, they are mobile and repelled by each other due to electrostatic force. The agglomeration at the surface leads to a slightly negative surface charge, which causes a small electric field outside the metal surface.

The aqueous electrolyte contains water molecules, which are electric dipoles, and solvated ions, which can freely move inside the solution. When the electrolyte gets in contact with the metal surface, the mobile ions and the water dipoles are attracted by the small electric field according to electrostatics. Consequently, the metal surface gets covered with accumulating water dipoles and ions. This results in the formation of the *inner Helmholtz plane* (IHP), where mostly water dipoles and unsolvated ions exist, followed by the *outer Helmholtz plane* (OHP), where a layer of solvated ions is formed in the electrolyte. In combination, both layers form the *Helmholtz Double Layer* (HDL).
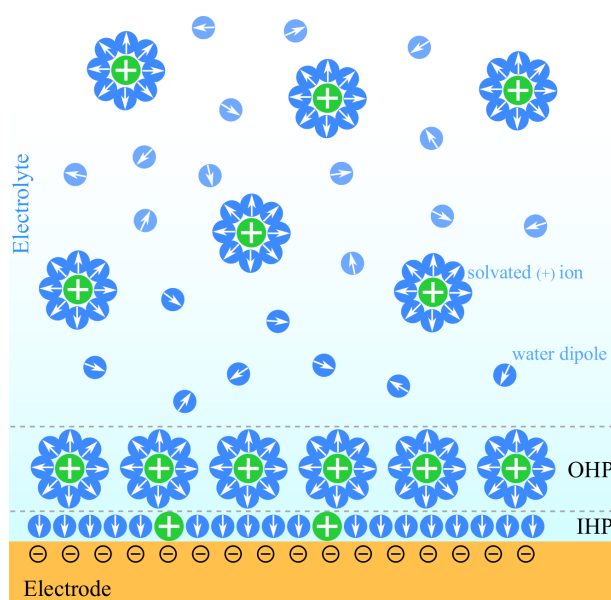

Figure 1.10: Schematic representation of the metal-electrolyte interface. The metal surface gets covered with water dipoles, that form the inner Helmholtz plane (IHP), and with solvated ions, that form the outer Helmholtz plane (OHP). Both planes build the electric double layer, which is termed Helmholtz Double Layer (HDL).

According to the model of Helmholtz, the HDL is basically a rigid layer of solvated ions near a metallic surface. Based on the separation of charges, this interface forms a capacitor, whose capacitance C_I is determined by the relative permittivity of the electrolyte ε_r, the permittivity of vacuum ε_0, the interface electrode area A and the distance of the OHP from the metal electrode d_{OHP}:

$$C_I = A \, \frac{\varepsilon_r \varepsilon_0}{d_{OHP}}. \tag{1.12}$$

Later, Gouy and Chapman modified the simple Helmholtz model by considering the solvated ions to be mobile at the metal surface. These mobile ions were influenced by thermal and electric effects, resulting in an ion cloud near the interface. In 1924, Stern combined both the Helmholtz and the Gouy-Chapman model: A layer of bound solvated ions in the OHP with a diffuse ion cloud beyond it [7], see also fig. 1.10.

The physical reactions and processes occurring at the interface are considered to be either *faradaic* or *capacitive*. A faradaic current describes the transfer of an electron across the interface from ionic to electronic conductivity or vice versa. This process is known as RedOx reaction at the surface, where for example a positively charged ion receives an electron from the metal and thereby undergoes a change in valence, called reduction, or vice versa, where a negative ion releases an electron to the metal, called oxidation. Capacitive coupling involves the charging and discharging of the metal-electrolyte double layer, due to a difference in potential, or the modulation of the capacitance due to changes in the electrolyte permittivity, by for example changes of ionic concentration.

These two processes happen simultaneously at the interface. To model these processes, we present an electrical equivalent circuit to gain deeper understanding of the interface behavior in the next section.
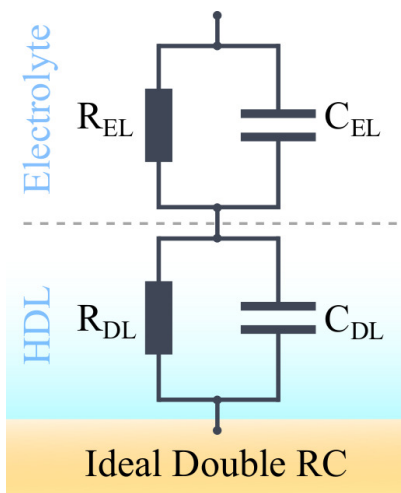
1.4.2 Equivalent circuit modeling

In the previous section we focused on the metal-electrolyte interface, where an electric Helmholtz double layer (HDL) is established. Physical reactions across the interface can be of faradaic or capacitive nature. Both processes happen simultaneously. Tho understand the electrical behavior of the metal-electrolyte interface, a model was developed that describes the electric properties of the double layer and the electrolyte as double RC equivalent circuit.

Figure 1.11 shows the equivalent circuit for an *ideal* interface with Helmholtz Double Layer (HDL), which consists of two RC circuits. The HDL and the electrolyte solution are each represented by one RC circuit.
In both RC circuits, a resistance is in parallel with a capacitor. For the HDL, the double layer capacitor C_{DL} is associated with the charging processes of the double layer due to changes in potential in the electrolyte. It is in parallel with the electric double layer resistance R_{DL}. For the electrolyte loop, R_{EL} represents the resistance of the electrolyte solution due to ionic conductivity. For the sake of consistency, we include the electrolyte capacitance C_{EL}, despite considering this capacitance to be zero or very small. We assume the double layer to dictate the electric properties of the double RC model.

For the description of the electric properties of the double RC equivalent circuit, the impedance for the double layer Z_{DL} and for the electrolyte Z_{EL} sum up to be the total impedance Z:

$$Z = Z_{DL} + Z_{EL}, \tag{1.13}$$

Figure 1.11: Double RC equivalent circuit to model the ideal Helmholtz double layer at the metal-electrolyte interface.

where the single components for each loop in the *ideal* double RC are

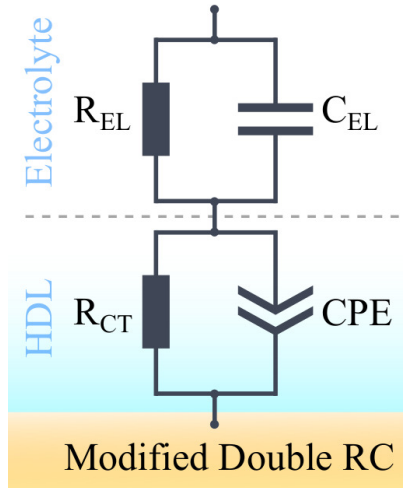$$Z_{EL} = \frac{1}{\dfrac{1}{R_{EL}} + i\omega C_{EL}} \tag{1.14}$$

and

$$Z_{DL} = \frac{1}{\dfrac{1}{R_{DL}} + i\omega C_{DL}}. \tag{1.15}$$

Based on experimental results from impedance spectroscopy, which will be presented later, we neglect the idea of C_{DL} being a *perfect, ideal* HDL capacitance. Thus, we modify the ideal equivalent circuit to obtain a more realistic model. The new RC circuit for the HDL includes the ohmic charge transfer resistance R_{CT}. The charge transfer resistance can be related to the discussed faradaic reactions and models the electrons moving across the metal-electrolyte interface when performing RedOx reactions. Moreover, the double layer capacitance in the circuit was changed to constant phase element CPE. The CPE describes an *imperfect* capacitor, whose impedance is frequency-dependent. The CPE is used to describe the dispersive behavior of the impedance of realistic electrodes in contact with electrolyte [11]. Unlike the regular expression for an ideal capacitor, the impedance of a constant phase element can be expressed as

$$Z_{CPE} = \frac{1}{(i\omega)^\beta \cdot C_{DL}} \qquad \Leftrightarrow \qquad \frac{1}{Z_{CPE}} = (i\omega)^\beta \cdot C_{DL} \quad , \qquad (1.16)$$

which is based on the double layer capacitance C_{DL}, but features an exponent that is typically $\beta \approx 0.8...1$. This exponent has been empirically related to the roughness of the electrodes, where $\beta = 0.5$ describes porous electrodes and $\beta = 1$ reflects ideally flat electrodes [11]. The RC circuit for the electrolyte is not modified. Referring to equation (1.16), the contributions of both RC circuits for the total impedance Z of the modified equivalent circuit result to be

$$Z_{EL} = \frac{1}{\frac{1}{R_{EL}} + i\omega C_{EL}} \qquad (1.17)$$

for the electrolyte as before and for the double layer

$$Z_{DL} = \frac{1}{\frac{1}{R_{CT}} + \frac{1}{Z_{CPE}}}$$

$$Z_{DL} = \frac{1}{\frac{1}{R_{CT}} + (i\omega)^\beta \cdot C_{DL}}. \qquad (1.18)$$

Figure 1.12: Modified double RC equivalent circuit, which includes the charge transfer resistance and a constant phase element to model a more realistic electrode behavior at the metal-electrolyte interface.

With this new approach, the low frequency electric behavior significantly differs from the Helmholtz model. The capacitance C for the overall equivalent circuit with total impedance Z can be calculated to be

$$C = \frac{1}{i\omega Z} \quad , \tag{1.19}$$

with respect to phase shift due to complex calculation. An example of the total impedance and capacitance for the ideal double RC (Helmholtz model) and the modified double RC (CPE model) in comparison to obtained data from impedance spectroscopy is shown in fig. 1.13. Therefore, both models were implemented in MATLAB, with the parameters for the electrical components specified in the graph. The simulation shown is of qualitative nature and demonstrates only one example of the great possibilities of the CPE model.

In fig. 1.13a we depict the simulated impedances of the equivalent circuits as a function of frequency, where the black curve represents the Helmholtz model and the red curve shows the result of the CPE model. In addition, 3 different curves for impedance are shown, which were obtained from an impedance spectroscopy measurement performed with a Solatron 1260 Impedance Analyzer. Therefore, the transducer, which is described in chapter 2, was subsequently filled with three solutions of potassium chloride (KCl) solution of different concentrations as specified near the curves.

It becomes apparent, that the simulated impedance of the Helmholtz model differs from the experimental data an can not sufficiently fit the data. In contrast, we achieved a set of parameters for the CPE model, that results in a fit which is in acceptable agreement with the measured impedance of the transducer.

Relating to eq. (1.19), we present the calculated capacitance curves for the same parameters and measurements in fig. 1.13b. Here, the strong derivation of the Helmholtz model from the experimental capacitance data is clearly observable. With this basic model, the dispersive behavior in measured capacitance can not be modeled sufficiently. The CPE model in red results in a simulated capacitance curve, which is in good correlation with the obtained data. The shape of the capacitance curve with 500 mM KCl can be fitted accurately with appropriate simulation parameters for the CPE element.

In this section we presented our approach to model the electric properties of the metal-electrolyte interface to investigate the relevant processes at the microelectrodes in the transducers in the future. The comparison of the two different models and the measured data validates the idea of modeling the electrical interface behavior with the CPE approach. The modified double RC equivalent circuit is in good correlation with the measured results when choosing a suitable set of parameters. However, the nature and behavior of the CPE model is not yet sufficiently understood, why many more experiments for transducer characterization and modeling have to be performed in future work. Ultimately, this methodology of 'model-testing' leads to improved knowledge on metal-electrolyte interfaces as well as the transducer itself.
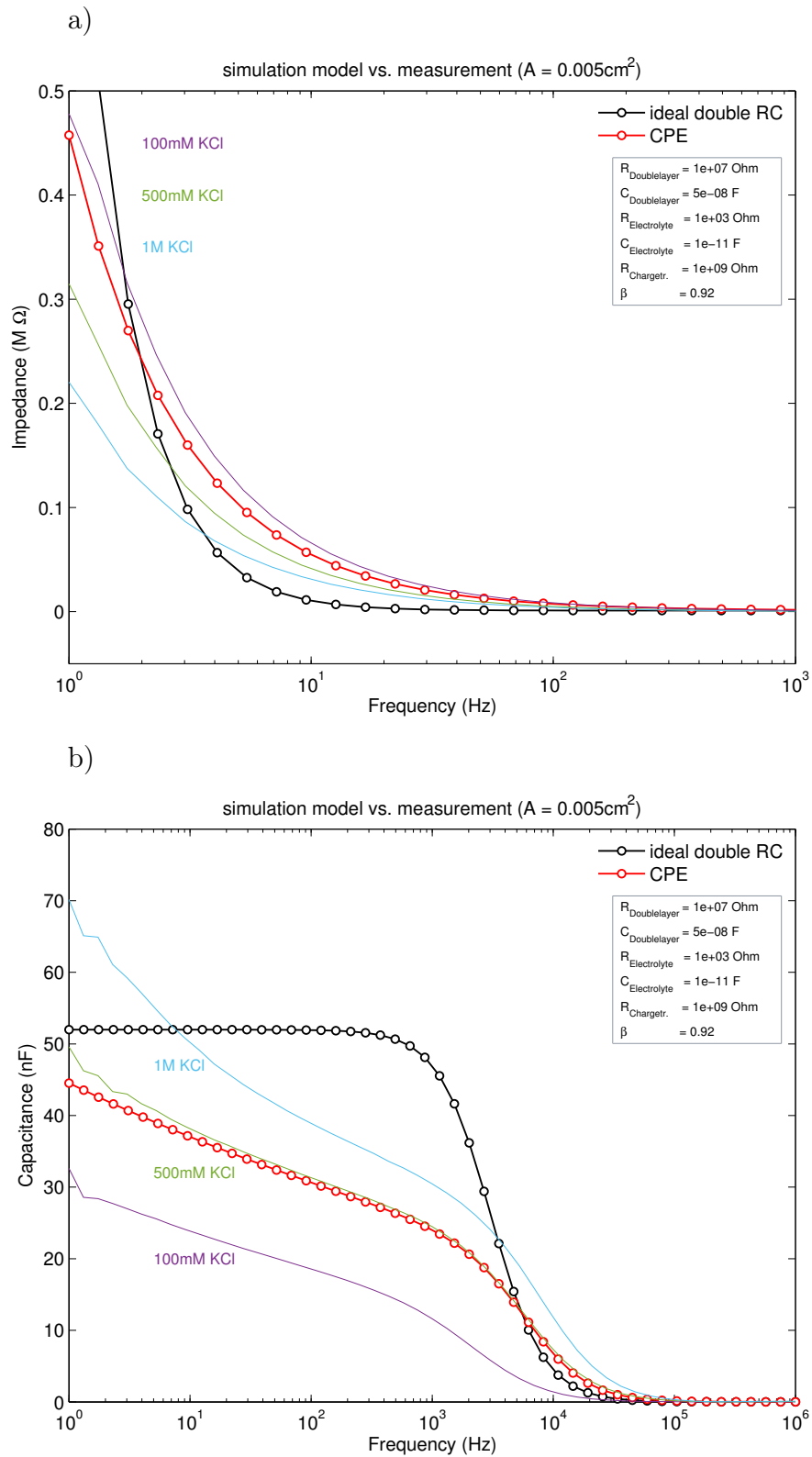
a)

b)

Figure 1.13: Comparison of simulation and measured data for impedance and capacitance. a)
Simulated impedance of the Helmholtz model (black) and the CPE model (red). b) Simulated
capacitance according to a). In both plots, the Helmholtz model deviates clearly from the
experimental data, but the CPE model results in fit curves that are in good agreement.

2 Transducer fabrication

In this section, we depict the fabrication process of newly developed transducers for detection and recording of bioelectronic signals in cell populations. We designed two different electrode geometries to investigate different parameters, like for example the effect of for example electrode size, on the electric properties. The transducing electrodes were manufactured using gold vapor deposition on glass substrates, which included the fabrication of brass shadow masks of two different geometries. Prior to the gold deposition, the glass substrates were thoroughly cleaned following a fixed protocol. The transducers were equipped with a PMMA compartment to receive the cell populations and the culture medium on top. Moreover, a device holder was designed, that supports the transducers and connects the particular electrodes to the peripheral measuring equipment.

2.1 Microelectrode design

For the investigation of the effects of electrode size on the electrical characteristics of microelectrodes for bioelectronic measurements, we started with the design of four different electrode geometries for transducer fabrication. The electrode sizes are 0.005 cm^2, 0.01 cm^2, 0.1 cm^2 and 0.78 cm^2.

The size of the transducers is determined by the given dimensions within the fabrication process, like for example the available glass substrate size. Therefore, we split the electrode geometries and designed two types of different transducers.

Firstly, *Type A* transducer design features the smaller electrodes of different electrode size, which are equally spaced 4 mm apart from each other. Secondly, *Type B* transducer design contains a single electrode of 0.78 cm^2. All electrodes have a bonding pad attached, where the can be connected to peripheral equipment.

The electrode fabrication was performed by gold vapor deposition. Therefore, brass shadow masks were manufactured using computer assisted milling cutter technique. The masks determine the electrode geometry in the deposition process. The two masks with different electrode geometries are shown in fig. 2.1.
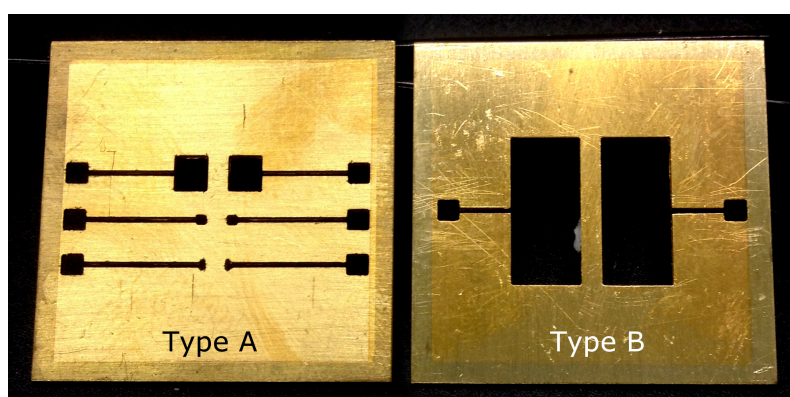

Figure 2.1: Brass shadow masks for gold deposition. Type A features electrode size 0.005 cm^2, 0.01 cm^2, 0.1 cm^2 and 0.78 cm^2, Type B is for electrode size of 0.78 cm^2.

2.2 Fabrication process

The fabrication of novel microelectrode transducers on glass substrates requires advanced manufacturing procedures and a high level of cleanliness to obtain excellent results. Fortunately, MPIP facilitates all of the necessary equipment for cleaning and evaporation techniques, which allowed autonomous in-house manufacturing of new transducers.

For the fabrication of new chips, plate glass substrates were provided by in-house glass manufacture, with dimensions of $30\,\text{mm} \times 30\,\text{mm} \times 1\,\text{mm}$. The production process can be divided into two general steps, which are firstly the cleaning procedure and secondly the evaporation of the electrodes. The applied cleaning protocol will be presented in the following. The finalized chips were equipped with a PMMA compartment to hold the culture medium and the cells. Lastly, the chips were mounted in a device holder for electrical connection to the peripheral measuring equipment.

2.2.1 Cleaning and evaporation procedure

For the evaporation of gold electrodes, it is crucial to use very clean glass substrates. At first, the substrates were checked for defects by eye. When not in use, the glass substrates were stored in an air tight container all the time to prevent contamination. The following cleaning protocol was fixed for all substrates and ensures a sufficient level of cleanliness. The particular steps were:

1. Substrate soaking in 50/50 vol-% Extran soap/water mixture, followed by substrate rubbing with soap by hand for about 2 minutes from both sides, to remove residual dirt and dust particles.

2. Substrate rinsing in millipore (type 1) water twice to remove the soap.

3. Substrate rinsing in a sample holder immersed in acetone.

4. Acetone sonication bath for 5 minutes.

5. Substrate rinsing in isopropanol.

6. Isopropanol sonication bath for 5 minutes. The ultrasonic bath helps to degas the substrate and removes residual water and particles.

7. Substrate drying thoroughly in high pressure nitrogen beam to evaporate the residual isopropanol.

The cleaned substrates were placed in the vacuum chamber of the deposition controller. Therefore, the masks were put underneath the glass substrates inside a sample holder and the chamber was pumped down to approximately $1 \cdot 10^{-6}$ mbar. When the final pressure was achieved, the thermal evaporation deposition was performed in manual mode. Firstly, a 2 nm chromium layer was deposited as gold adhesion layer. Secondly, gold was deposited according to the desired thickness. In this work, gold layers with thickness of 20 to 240 nm were realized. The gold deposition rate was 15 Å/s. The overall roughness of the electrode surface increases with higher thickness of the gold electrodes [12]. Increasing the deposition rate leads to a rougher gold surface, while a decreased rate leads to smoother gold films. A substrate after the gold deposition is shown in fig. 2.2a. The finalized transducer with PMMA compartment is depicted in fig. 2.2b.
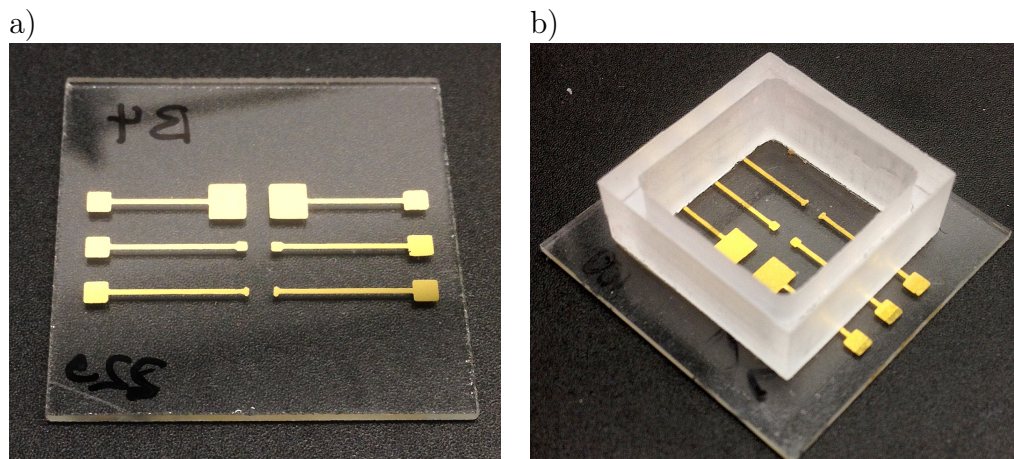

Figure 2.2: a) Fresh chip of Type A design after gold deposition on glass substrate.
b) The finalized transducer with glued PMMA compartment to hold the fluid.

2.2.2 Transducer assembly and handling

After the deposition procedure, the fabricated chips with different gold electrodes were stored in a box to avoid contamination. For a measurement, one chip was prepared with a tub to hold the culture medium and the cells on top of the transducer. Therefore, a quadratic PMMA compartment was glued on the active side of the substrate with double-sided adhesive tape (fig. 2.2b). It was important to apply high pressure by hand to ensure proper sealing of the transducers.

For reliable and steady electrical connection of the transducers, a device holder was designed. This holder consists of a socket and a cover made from Teflon (PTFE). In between one in-house chip can be mounted and fixed with screws, shown in fig. 2.3a. The electrical connection was realized by vertically arranged gold contact springs, which apply a constant force to the gold connection pads of the chips (see also fig 2.2a,b). Fig. 2.3b shows an empty chip mounted in the holder, which was placed in a metal box. Each electrode pair is connected to one BNC connector inside the box and therefore accessible separately. The box with the holder inside is mounted inside the incubator, where low noise cables lead to the measurement equipment. This holder is beneficial for all measurements with different electrode areas. The advantage is that each electrode pair can now be probed without accessing the box or the transducer itself, which strongly disturbs the measurement.
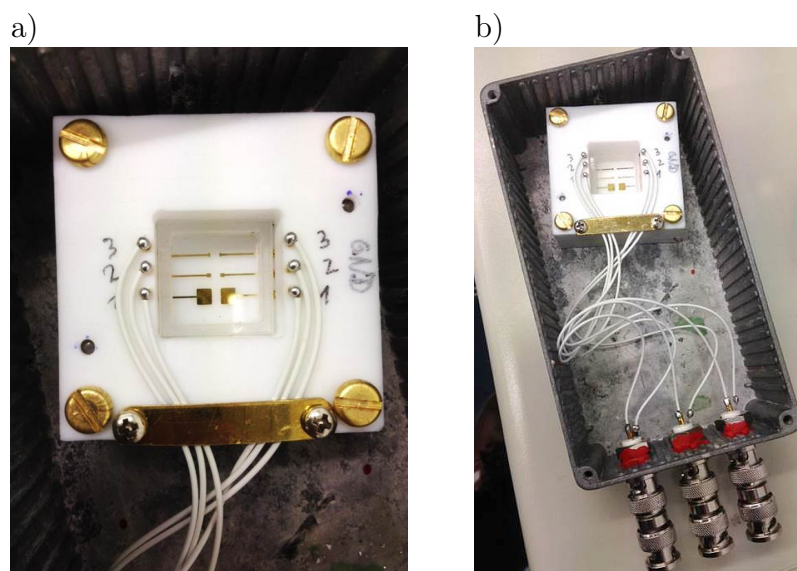
a)   b)

Figure 2.3: a) A device holder was designed for proper connection and handling of the transducer. It ensures a steady electrical connection of all 3 electrode areas to the peripheral measuring equipment. b) Device holder mounted in metal box, which can be connected inside the incubator.

3 Experimental setup for bioelectronic measurements

In this chapter, we present the experimental setup and methods for measurements of bioelectronic activity of cell populations over a long time. Therefore, we depict the instrumentation necessary for highly sensible low noise current measurements and present different operational aspects of the used equipment. Moreover, a data acquisition software for long-term data recording was written in LabVIEW. Lastly, information on cell culturing is provided.

3.1 Instrumentation for current measurements

Here we describe the different components of the employed measuring equipment for low-noise current recordings. We use two different types of transducers. In the beginning of this work, measurements of C6 glioma cells were performed using a commercial sensing device, which is shown in the next section. Later, we started the in-house fabrication of newly developed transducers as depicted in in chapter 2, that were used for the measurements of a neuron population. The results will be presented in chapter 4.

The transducers were mounted inside a metal box and placed in an incubator, which provides ideal physiological conditions for the maintenance of cells. The transducer inside the incubator was connected to a low-noise current preamplifier. The current signals were digitalized by a signal analyzer. Since the peripheral measuring equipment is highly sensitive in the femtoampere range and therefore susceptible for parasitic electromagnetic crosstalk, it was placed inside a Faraday's cage for shielding. Special low-noise cables were thoroughly used for electrical wiring.

The final arrangement of all equipment in our laboratory is shown in fig. 3.6.

3.1.1 Commercial transducer (Philips)

The initial sensing device was developed as a metal/Si/SiO$_2$ based transistor-like structure and fabricated using lithographic processing by Philips Innovation Services (Eindhoven, Netherlands). The transducers on one silicon wafer, 150 mm in diameter, have to be separated by breaking the single chips apart from each other, followed by cleaning in high-pressure nitrogen beam to remove scattered silicon particles and dust.

Every chip contains four bidirectional transducer lines equally spaced 4 mm apart from each other, see fig. 3.1a. The transducers are interdigitated gold microelectrodes fabricated on top of 190 nm thermally oxidised silicon (SiO_2). One electrode pair consists of five interdigitated pairs of gold strip lines, with bonding pads at both ends for electrical connection.
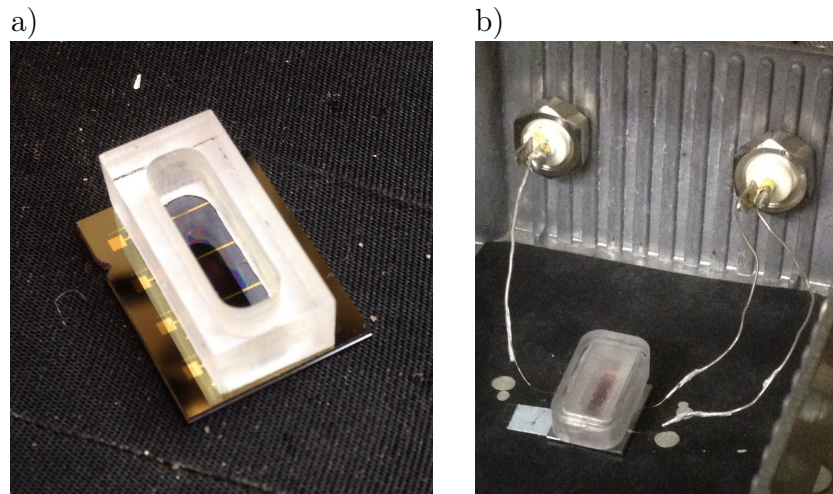

Figure 3.1: a) Commercial sensing device from Philips with glued PMMA compartment. The transducer contains 4 electrode pairs. b) The transducer with PMMA lid to prevent medium evaporation mounted in the metal box.

On top of the chip, a PMMA compartment is glued using double-sided tape. Its volume is 250 μL. This compartment is to be filled with culture medium and cells. To prevent evaporation of the culture medium, the compartment is covered with a accurately fitting PMMA lid.

The transducer and the containing cells have to be protected from ambient parasitic impacts. Therefore the chip is mounted inside an enclosed black metal box, similar to the box shown in fig. 2.3b, which also enables safe handling of the sensing unit. The box is equipped with two BNC-connectors, with attached flexible silver wires leading towards the chip inside the box. For measuring and recording, the two bonding pads of *one* inner transducer line are connected to the silver wires with thin gold wires and silver paste, which is shown in fig. 3.1b.

3.1.2 Incubator

The transducer system inside the box was put in an incubator (Thermo Scientific ® Midi 40) to ensure ideal biological conditions. The incubator maintains an appropriate atmosphere for living cells at $37\,^{\circ}C$ with 5% of CO_2. To ensure sufficient supply of CO_2, the lab was equipped with a cabinet, which holds two gas cylinders. These are connected to a gas supply panel, which automatically switches to a new feeding cylinder in case of low filling level.

This incubator was modified to mount the metal box with the transducer inside. Therefore, the incubator was equipped with BNC ports at its inner back plane, which allows the connection of the box for measurements. There are two sites for connections available. The main site for measurements is located in he lower middle of the incubator for good accessibility of the box and the transducers. This spot features 3 female BNC connectors and enough space for i.e. culture medium change, transducer adjustments or experiment manipulation (drug delivery etc.). The second site is located near the ceiling and features two BNC connectors. For manipulation of a measurement, it is necessary to disconnect the box, why this site was used mostly for secondary measurements (i.e. control, comparison, baselines).

Before starting a long-term measurement with living cells, the inside of the incubator was thoroughly cleaned with > 70% Ethanol. A petridish with a mixture of fungicide and ultrapure water was placed below the metal shelf. This procedure helps to avoid contamination with bacteria or fungus inside the incubator during a measurement. It also humidifies the atmosphere and thus prevents fast evaporation of the cell's culture medium.
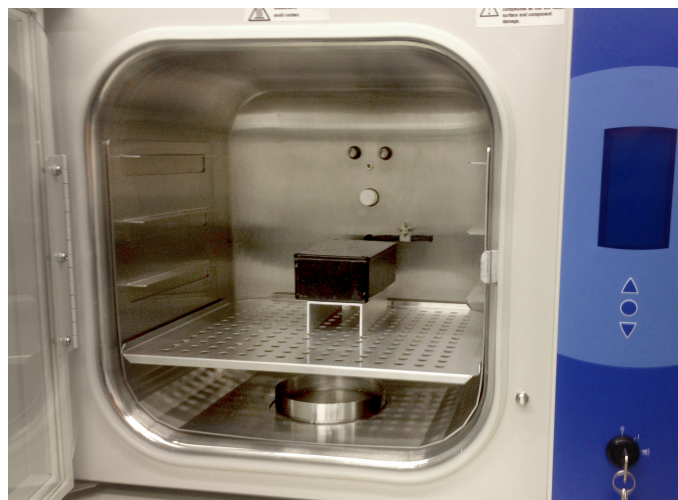

Figure 3.2: Thermo Scientific Midi 40 CO_2 Incubator (open) with mounted metal box, that contains the transducer with the cells.

3.1.3 Preamplifier and bandwidth

The wiring inside the incubator enables transfer of the cell's bio-electronic signals to the peripheral measuring hardware. Hence, low-noise coaxial cables are used to connect the transducer to a low-noise current amplifier (Stanford Research Systems SR570).
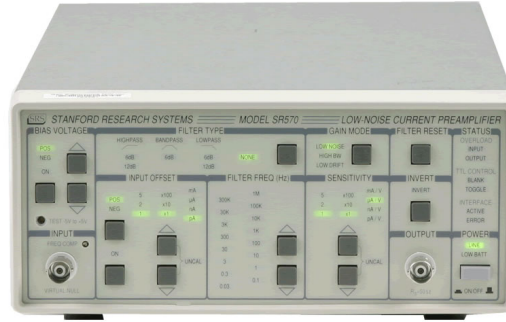

Figure 3.3: SR570 low-noise current preamplifier
(www.thinksrs.com, author unknown).

This highly sensitive current preamplifier is able to detect marginal current fluctuations within the transducing system in the range of femto-Ampere when used with appropriate settings. The SR570 provides a voltage output proportional to the input current. Sensitivities range from 1 mA/V down to 1 pA/V. It operates with a floating ground with the amplifier ground isolated from the chassis and the AC power supply. It can run on internal batteries, but as the power supply in the lab is quite clean, it was possible to perform the measurements on AC power.

The internal current noise of the SR570 varies depending upon the amplifier's settings. As we expect the cells to produce minute current fluctuations, it is desired to decrease the noise contribution of the amplifier to a minimum for proper detection. For this purpose, the amplifier was set to *Low Noise Mode*, with selected sensitivities in the range of $S = 1...100\,\mathrm{nA/V}$, depending on the particular measurement.

These parameters, namely mode and sensitivity, do highly effect both bandwidth and current noise of the amplifier, which is depicted in fig. 3.4. Following Johnson-Nyquist noise, as mentioned in section 1.2.1, the current noise of the system is given by:

$$I_{noise}(rms) = \sqrt{\frac{4\,k_b\,T\,df}{R}}, \tag{3.1}$$

where k_b is the Boltzmann's constant ($1.38 \cdot 10^{-23}\,\mathrm{J/K}$), T is the temperature in Kelvin, R is the resistance in Ohms and df is the bandwidth of the measurement in Hz. Consequently, the selected sensitivity and therefore the bandwidth determines the intrinsic current noise of the amplifier. One has to be aware that changing the mentioned parameters will affect the measurement.

Aside from smart circuit design, such a high sensitivity is also achieved by reducing the amplifier's bandwidth according to eq. (3.1). Using *Low Noise Mode* with for example $S = 1\,\mathrm{nA/V}$, the current noise is located in the range of 10...60 fA, which is quiet low, see fig. 3.4.

When measuring for example glioma cells, this sensitivity enhances the *signal-to-noise ratio* (SNR) to a sufficient level, as a typical cell membrane's current noise fluctuation level (signal) is found within 200 fA...5 pA. Furthermore, the input signal is low-passed at cutoff frequency $f_c = 15\,\mathrm{Hz}$ according to figure 3.4a, which is beneficial for the detection of the signals of interest. When performing these ultra low-noise measurements, the low-pass filtering efficiently reduces parasitic effects like 50 Hz hum and interfering high-frequency stray signals.
On the other hand, when the input signal is too large, the amplifier will indicate a signal overload. This has to be avoided, as it will drastically lower the quality of the measurement. To keep the input signal within the dynamic reserve of the amplifier, which is typically 33 dB, a lower sensitivity of for example $\sim 100\,\mathrm{nA/V}$ has to be selected when performing measurements with higher current output (e.g. neurons), as the input signal cannot be changed. This leads to more spectral information due to a higher bandwidth on one hand, but therefore increases the amplifier's noise on the other. Thus, selecting appropriate settings for a particular measurement is always a trade-off between acceptable signal-to-noise ratio and the accessible bandwidth.
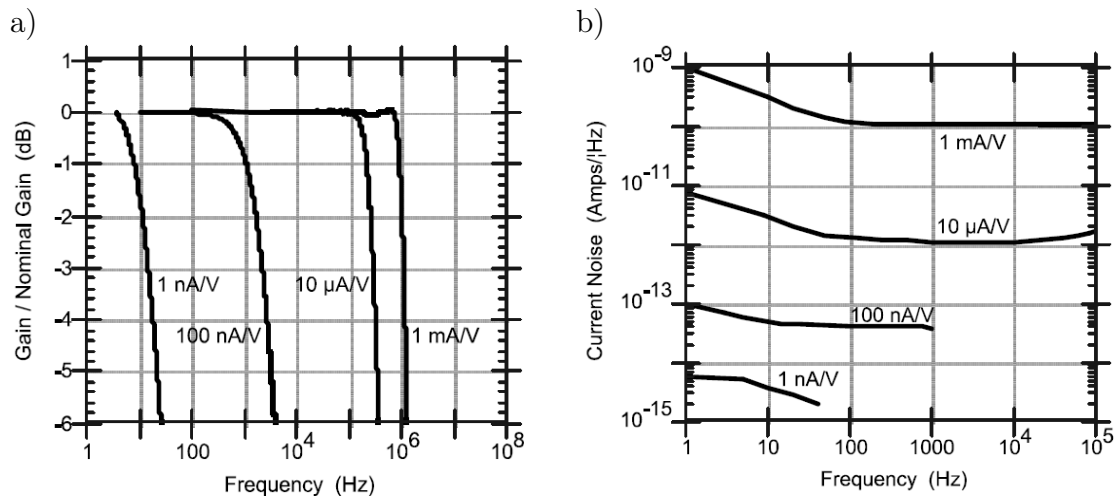

Figure 3.4: Amplifier bandwidth (a) and current noise (b) as a function of frequency (from SR570 manual).

3.1.4 Signal Analyzer and digitalization

The output signal of the current preamplifier is an analog DC voltage, which is proportional to the input current and scales with the amplifiers sensitivity. For example, assuming a sensitivity $S = 1\,\mathrm{nA/v}$ and an input current $I = 1\,\mathrm{pA}$, we can calculate the expected output voltage of the current preamplifier V_A using the definition for sensitivity:

$$S = \frac{I}{V_A} \quad \Leftrightarrow \quad V_A(1\,\mathrm{pA}) = \frac{I}{S} = \frac{1\,\mathrm{pA}}{1\,\mathrm{nA/v}} = \frac{10^{-12}\,\mathrm{A}}{10^{-9}\,\mathrm{A/v}} = 10^{-3}\,\mathrm{V} = 1\,\mathrm{mV}. \qquad (3.2)$$

It becomes apparent that small input current noise fluctuations from e.g. glioma cells around $200\,\mathrm{fA}...5\,\mathrm{pA}$ lead to minute changes of the amplifier's output voltage in the range of $200\,\mu\mathrm{V}...5\,\mathrm{mV}$. These minor voltage changes are to be recorded and thus digitized accurately for precise measurements and further signal analysis procedures.

For the purpose of high quality A/D conversion, the preamplifier's output was connected to a highly sensitive *Dynamic Signal Analyzer* Agilent 35670A. The analyzer's input signal resolution is in the range of $\pm\,5\,\mu\mathrm{V}$, which represents a detection limit of $\pm\,5\,\mathrm{fA}$ when using highest sensitivity $1\,\mathrm{nA/v}$. With these specifications, this analyzer is most suitable for precise recording of the cell's bioelectronic activity.

Figure 3.5: 35670A Dynamic Signal Analyzer
(www.keysight.com, author unknown).

The analyzer was used in *FFT Mode*, hence it displayed both the recorded time course $V_I(t)$ and the derived noise spectrum $S_V(f)$. The signals were recorded with two different sampling rates $f_s = 16\,\mathrm{Hz}\,/\,64\,\mathrm{Hz}$. According to Nyquist, the upper frequency limits then are

$$f_{max} \leq 0.5 f_s = \begin{cases} 8\,\text{Hz} & for\ f_s = 16\,\text{Hz} \\ 32\,\text{Hz} & for\ f_s = 64\,\text{Hz} \end{cases} \tag{3.3}$$

in theory. To provide a reliable confidence interval, the analyzer actually calculates the upper frequency limit according to

$$f_{max} = 0.39 f_s = \begin{cases} 6.25\,\text{Hz} & for\ f_s = 16\,\text{Hz} \\ 25\,\text{Hz} & for\ f_s = 64\,\text{Hz} \end{cases} \tag{3.4}$$

The low frequency limit f_{min} is determined by the selected recording length T_R for one measurement, which was set to 64 s. Within this time window, the analyzer captures the time trace of the selected input channel $V_I(t)$ and then performs the spectral analysis from the obtained data. The minimum frequency which is detectable by the FFT analysis is given by

$$f_{min} = \frac{1}{T_R} = \frac{1}{64\,\text{s}} = 0.015625\,\text{Hz}. \tag{3.5}$$

With these settings, the analyzer provides a credible low-frequency bandwidth BW

$$BW = \begin{cases} [15.625\,\text{mHz}\,,\,6.25\,\text{Hz}] & for\ f_s = 16\,\text{Hz} \\ [15.625\,\text{mHz}\,,\,25\,\text{Hz}] & for\ f_s = 64\,\text{Hz} \end{cases} \tag{3.6}$$

for spectral analysis. These intervals describe the frequency range of the *analyzer's* FFT analysis. For more detailed spectral analysis, we investigated distinct methods in MATLAB, which will be discussed later.

Performing a measurement, the analyzer records 64 s of the incoming voltage signal and calculates the voltage spectrum $S_V(f)$. Depending on the samplingrate, the amount of recorded samples n per time window is

$$n = \begin{cases} 16\,\text{s}^{-1} \times 64\,\text{s} = 1024\,\text{samples} & for\ f_s = 16\,\text{Hz} \\ 64\,\text{s}^{-1} \times 64\,\text{s} = 4096\,\text{samples} & for\ f_s = 64\,\text{Hz}. \end{cases}$$

Both plots are shown on the display. The analyzer was set so average 25 measuring cycles to achieve a smoothed resulting spectrum. Both traces can be manually saved to the analyzer's internal memory and later read back from the computer via GPIB interface.

According to 3.1.3, the incoming voltage represents a measured current. With respect to the selected sensitivity S of the preamplifier, we therefore consider the measured voltage time course $V_I(t)$ and the corresponding voltage spectrum $S_V(f)$ to represent the current time course $I(t)$ respectively the current spectrum $S_I(f)$ in the transducer. According to eq.(3.2), we obtain:

$$I(t) = S \cdot V_I(t) \tag{3.7}$$
$$S_I(f) = S^2 \cdot S_V(f). \tag{3.8}$$

This conversion will be performed in the data acquisition software, which will be discussed in section 3.2.

3.1.5 Procedures for achieving low-noise current measurements

With our measuring system, we target low-noise current measurements sensitive in the femtoampere range. To obtain reliable results with such sensitivity, special procedures are necessary to avoid disturbing impacts of present electromagnetic stray fields. These parasitic stray fields originate mostly from regular power lines, that produce 50/60 Hz hum, but also from other electronic equipment like mobile phones or lamps etc.

A practicable method to avoid such parasitic effects is electromagnetic shielding by solid metals. Therefore, we mount the transducers, that, with their gold electrode lines, act like antennas, inside a metal box shown in fig. 2.3. For a measurement, the box with the transducer inside is placed inside the incubator, which is made of metal parts and therefore also features a certain level of shielding.

Inside, BNC lead to the outside of the incubator. The installed BNC connectors are insulating type, which prevents electric connection of the BNC shielding with the incubator or any conductive material outside the measurement box. Outside the incubator, ultra-low-noise cables connect the transducer to the peripheral measuring equipment. Additional metal mesh liners encase the low-noise cables.

All of the peripheral measuring equipment, which are the preamplifiers and the signal analyzer, are surrounded by a big metal box that act as Faraday's cage and therefore shields the equipment and the signals of interest against inevitable electromagnetic interference and stray capacities. The arrangement of the experimental setup in our lab is shown in fig. 3.6.
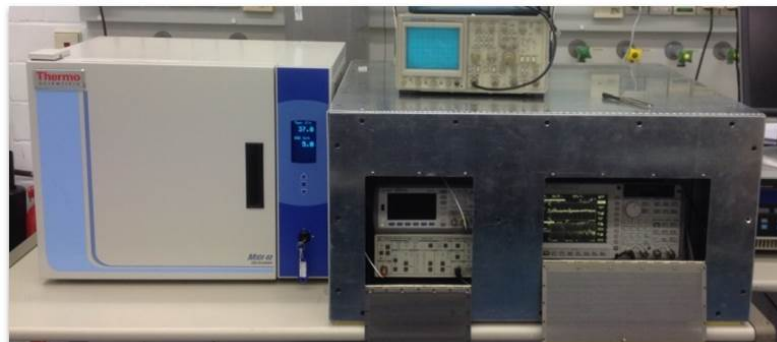

Figure 3.6: The arrangement of the experimental setup in our lab, with incubator and Faraday's cage, that contains the preamplifier and the signal analyser.

3.2 Data acquisition and long-term recording (LabVIEW)

For convenient data acquisition (DAQ), a customized software application was written and designed in LabVIEW. Its main purpose is the data transfer and storage of the obtained signal(s) from the Agilent analyzer. Therefore, the software features common functions of the DAQ-procedure like initialization of the analyzer, selecting measurement paths, GPIB transfer of the data, data logging and measurement control via GPIB.

With this software, the measurement can be operated from the computer without accessing the analyzer inside its Faraday's cage. This is convenient as the functions for autoranging and calibration can be executed remotely, which does not disturb the measurement. Moreover, this software now enables the long-term current recording (hours, days, weeks), which is a major advantage compared to the manual operation mode as before. The study of long-term evolution of bioelectronic activity in cell populations *in vitro* is now possible.
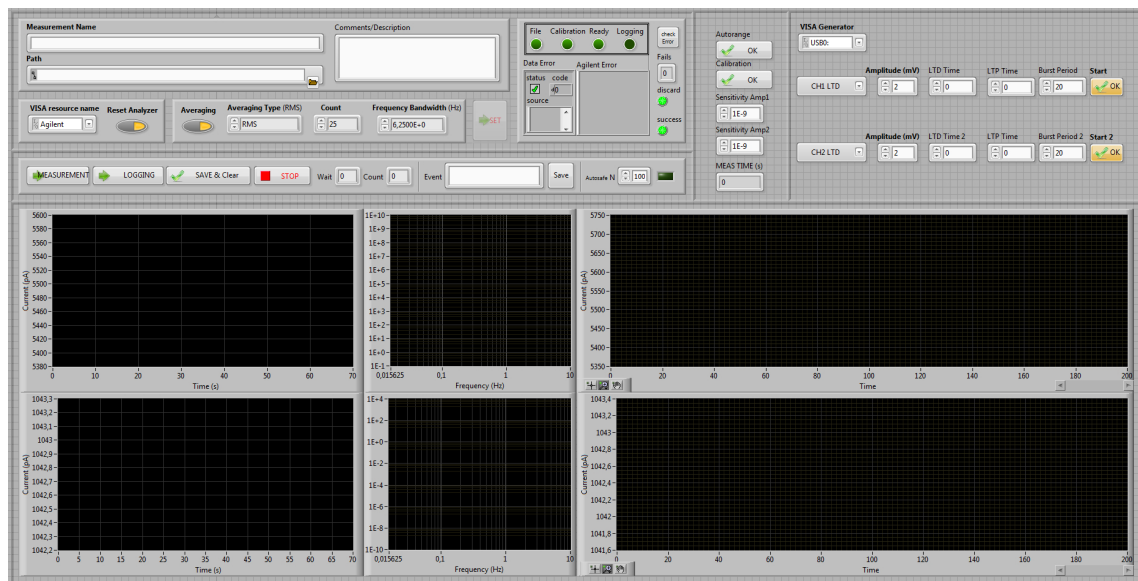

Figure 3.7: Frontpanel of the data acquisition software written in LabVIEW. In the upper left section the general settings for the measurement and analyzer are located like file path, averaging count, bandwidth. In the top center error section, calibration features and sensitivity can be adjusted. The graphs show from left to right the actual measured data, the current spectrum and the appended all-time current of the running measurement for channel 1 (up) and channel 2 (down).

This software is operated by a *Frontpanel*, which is shown in fig. 3.7. Actually, it features 2 channel data logging with selectable bandwidth up to 25 Hz. Before starting a measurement, the user can set the measurement name and path in the upper left corner. Comments on the particular experiment can be added. After setting the parameters for averaging type, bandwidth, frequency resolution and the sensitivity of the preamplifier, the analyzer is started by clicking the *set* button. Simultaneously, a new folder and 3 *.txt*-files for the measurement are created on the hard disk drive. The file names are coded with the date and measurement name as follows:

- *Date_ MeasurementName_ alltime_ CH1.txt*:
  for time and current values for channel 1
  (10 digits floating point in scientific notation)

- *Date_ MeasurementName_ alltime_ CH2.txt*:
  for time and current values for channel 2
  (10 digits floating point in scientific notation)

- *Date_ MeasurementName_ config.txt*:
  contains the header with the selected parameters, timestamp of the measurement, comment section, special events like autosave, autorange and manually created events (i.e. medium change)

Subsequently, the initialization phase includes the reset, calibration and setting of the analyzer. It receives all relevant GPIB commands according to the selected parameters. When the initialization is finished, the analyzer waits for the user to start the data acquisition. In the frontpanel, the *run* button starts blinking and thereby indicates a successful initialization.
When clicking the *run* button, the analyzer starts to capture data after a short settling phase. When 64 seconds of data have been recorded, it calculates the spectrum of this data. Both the time trace and the corresponding FFT spectrum are displayed on the analyzer's display. The next time capture starts immediately. When the received signals are reasonable and satisfying, the user can start the data logging and transfer to the computer by clicking the *logging* button. The full data captured by the analyzer is transferred via GPIB communication and plotted in the frontpanel, see fig. 3.7. Now, the analyzer is in continuous mode. The capture will be repeated sequentially and the data will automatically be transferred to the computer every 64 seconds by the running software.

While the measurement is running, the user can operate several features to control and modify the experiment:

- The measurement can be stopped by un-clicking the *logging* button for i.e. changing the culture medium, check the connections and the state of the cells etc.

- Particular events or interesting observations can be manually logged with the *Event* -window in the *config* file (for example medium change, spikes etc.)

- The analyzer can be calibrated or auto-ranged in case of signal overload without disturbing the measurement

To guarantee secure data logging when performing a long-term measurement, it is essential to store the actual data continuously on the hard disk drive. Considering a 10 day-experiment, the data must not be stored only in the computer's RAM until the experiment is finished for security reasons. For example, a breakdown of electricity would lead to total loss of data. Therefore, the previously created files are opened at the beginning of the data logging. When a recording cycle is finished after 64 seconds, the software appends the time and current values directly within the according file during the measurement. If now the measurement crashed for any reason, at least the previous signals were saved in the files.

In LabVIEW, an application (or "virtual instrument") consists of two parts: the frontpanel and the block diagram, which contains the actual source code. As the developed software is rather complex, the source code is not shown and discussed here. It can be found in the appendix.

3.3 Cell culturing and care

Rat glioma C6 cells (American Type Culture Collection, ATCC) were cultured in DMEM/F12 (with 15% of fetal horse serum and 2.5% of fetal bovine serum (FBS)). Human cervix carcinoma HeLa cells were cultured in DMEM (with 10% of FBS). All culture media were supplemented with L-glutamine and penicillin/streptomycin. Cells were maintained at $37\,°C$ in an incubator with a humidified atmosphere with 5% of CO_2. Upon cell detachment using trypsin/EDTA, cell numbers and viability were assessed using a Neubauer chamber-based trypan blue live/dead exclusion assay. An aliquot of 250 µL of culture medium containing 400.000 cells was transferred to the well of the transducer. Cells were allowed to sediment for 2 h before any measurements were performed.

Primary embryonic hippocampal neurons were provided from E18 wildtype embryonic laboratory mice by Universitätsmedizin Mainz. The protocol for cell extraction can be found in appendix. For the long-time measurement, 400.000 neurons were seeded on the in-house transducer directly after extraction and incubated for two days. Full neurobasal medium was changed every second day.

Prior to cell deposition, all devices were coated with poly-L-lysine (Sigma Aldrich) to promote cell adhesion for about 30 minutes.

4 Bioelectronic activity of cell populations

In this chapter, we present the results of current recordings from cell populations, which we obtained by means of the experimental setup depicted in the previous chapter. Prior to results of cell population recordings, we show the detection limit of our setup in the picoampere range.

First, we depict the results of experiments with C6 glioma cells and demonstrate the suitability of our system to record bioelectronic activity of cell populations in general. By means of specific chemical agents, we were able to unambiguously demonstrate that the obtained current signals are dominated by the flow of Na^+ and K^+ ions through voltage-gated ion channels.

Second, we show the evolution of bioelectronic activity within a primary neuron population in a long-term measurement of about two weeks. In this experiment, murine embryonic neurons were seeded in our in-house transducer. The maturing neuron population established a complex network with a high level of connectivity, that was observed with optical microscopy. We depict and discuss several interesting examples within the current signals, that exhibit features of inter-neuronal communication and therefore clearly approve the formation of a neuronal network regarding their bioelectronic activity. Moreover, we introduce the method of spectrogram as a powerful tool for time-resolved spectral analysis of the recorded signals.

4.1 Detection limit of the system

The measurement of bioelectronic activity, by detection of cell membrane potential fluctuations, requires an extraordinary sensitive technical setup. In this section we demonstrate the detection limit of our system. The background noise level for an in-house transducer is presented in fig. 4.1. The black curve represents an empty transducer connected to the peripheral measuring equipment, with a background noise level of 100 fA. The transducer was then filled with $800\,\mu$L of $1\,\mu$M KCl solution. The according current signals of the three electrode areas in blue, orange and yellow show a current noise level of only 1.5 pA. This current noise level represents the baseline of our system and therefore the detection limit with the in-house transducers.
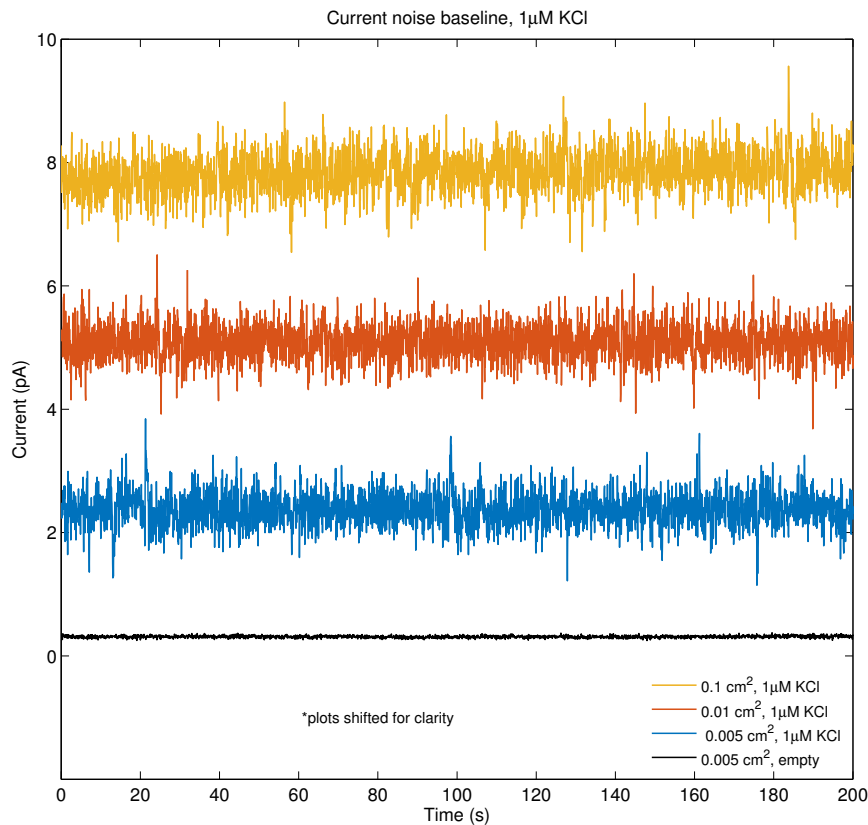

Figure 4.1: Current noise baseline signals obtained with the in-house transducer connected to the peripheral measurement setup. Here we show the current signals of the empty transducer (black) and the three electrodes that differ in size (blue, orange,yellow). The background noise is in the range of 1.5 pA.

For characterization and specification of this current noise, we analyze the measured current baseline signals in the frequency domain. Fig. 4.2 shows the calculated PSD curves of the recorded signals shown in fig. 4.1. The current noise spectra of the different electrode areas remain at a constant level of $10^{-2}\,(\mathrm{pA})^2/\mathrm{Hz}$ over the frequency range, despite of slight fluctuations are visible. All electrodes show a flat spectrum, which can be considered to be mainly thermal noise according to section 1.2.1. However, with increasing electrode area, the spectra show a slightly higher noise level in the low frequencies, typically below 2 Hz. The decrease of spectral magnitudes above 7 Hz is due to the characteristics of the current preamplifier, presented in fig. 3.4. The extremely low background noise level allows us to record even a minuscule bioelectronic activity, which we show in the next sections.
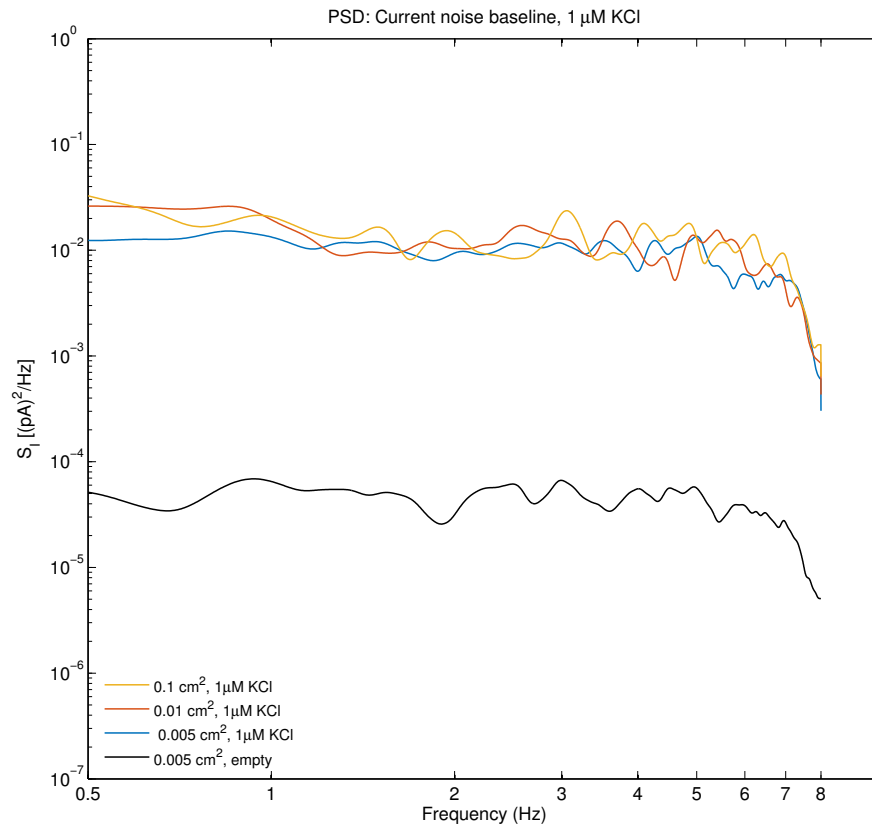

Figure 4.2: The detection limit of our system in current noise PSD spectra of the recorded current noise signal in fig. 4.1. The spectra show a flat curve from 2 Hz to 7 Hz.

4.2 Current noise in C6 glioma cells

In this section, we demonstrate the suitability of our system for the detection of bioelectronic activity within cell populations *in vitro*. This work has already been published in an article, *"Low frequency electric current noise in glioma cell populations"* [1]. In the following, we cite and conclude some of the results.

For this measurement, the commercial Philips chip presented in section 3.1.1 was used. Fig. 4.3a shows the baseline current signals compared to a signal recorded with C6 glioma cells. The blue curve represents the current noise level of a blank transducer around 100 fA. The orange curve displays the noise level of the transducer containing $250\,\mu$L of culture medium, which was 0.5 pA. As a kind of negative control we employed a human cervix carcinoma cell line from Henrietta Lacks in 1951, called HeLa, as these cells originated not from the brain or any other electrically excitable tissue. HeLa cells are known to be electrically quite. Due to the high sensitivity of our setup, even HeLa cells demonstrate fluctuations of their basal current level of around 3 pA (green curve), which is much higher in amplitude than the background acquisition noise. The yellow curve shows an examples of bioelectronic current signals obtained from C6 glioma cells.

The magnitude of the current fluctuations and the time evolution clearly differs between C6 and HeLa cells. As shown in fig. 4.3a, the current noise fluctuations of C6 glioma cells are much more pronounced and we could reproducibly detect and measure the current fluctuations.

These non-bursting, relatively prolonged changes in membrane potential, which we termed here as low frequency electric noise, are unlikely to be stochastic in nature. In fact, asynchronous current fluctuation of individual cells should largely cancel each other out, given the sufficiently high number of cells measured simultaneously. Instead, we propose that these current oscillations are either coordinated or occur simultaneously across our populations of roughly half a million of glioma cells.

In fig. 4.3b we show the current noise spectra S_I of the recorded bioelectronic signals in fig. 4.3a. Apart from the blue curve of the empty chip, all spectra clearly differ from thermal noise behavior. The spectrum of the culture medium, in orange, shows an increment in the frequency range above 3 Hz. The culture medium contains numerous types of nutrient substances and ions, which might contribute to a higher noise in this range. The spectrum of the basal, 'quiescent' electric activity of HeLa cells in green is significantly higher in magnitude compared to the culture medium. Thus, we confirm the ability of our system to detect minute membrane current fluctuations. In comparison to HeLa, the spectrum of the glioma cell signal in yellow is likewise higher in magnitude. According to the different type and level of the C6 glioma current fluctuations in fig. 4.3a, the corresponding spectrum represents their increased bioelectronic activity as well.

We have demonstrated that our sensing system allows non-invasive detection of

electrical activity of large cell populations of electrically quiescent and non-excitable cells (HeLa). Importantly, it also allows assessment of the spontaneous low frequency electrical noise in populations of glioma cells.
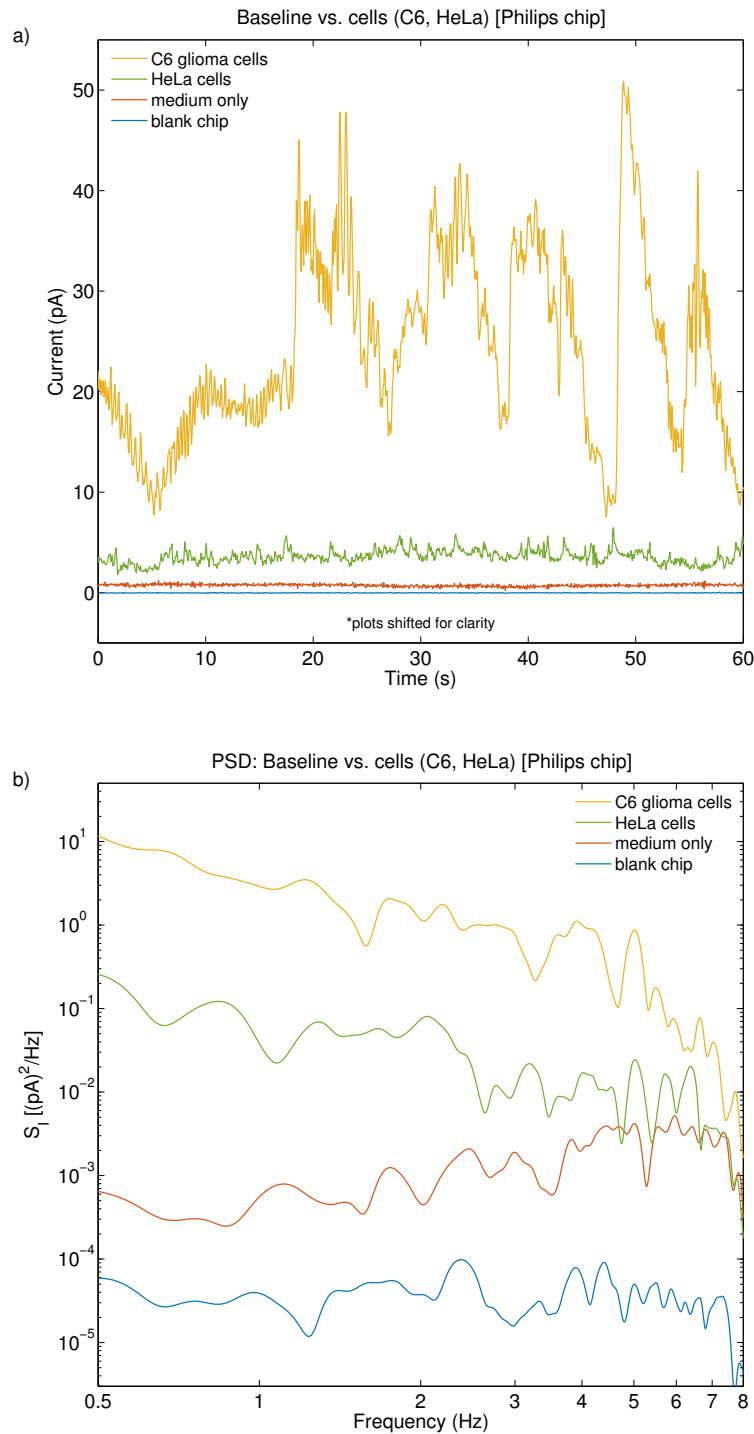

Figure 4.3: a) Biolelectronic current signals of different cell populations. The blue line represents the empty Philips chip, the red curve was recorded with only culture medium as baseline measurements. HeLa cells are shown in green. The yellow curve represents an example of the recorded current signals from C6 glioma cells. b) PSD spectra of the recorded bioelectronic signals in a).

In order to conclusively prove that our picoampere-range electric noise measurements do record actual membrane potential oscillations across a population of cells, we addressed the role of the relevant K^+ and Na^+ channels in the maintenance of electric population noise. Tetraethylammonium (TEA) ions are routinely used in neurophysiological studies to inhibit non-selectively across the wide range of K^+ channels, primarily of these protein families: the voltage-gated K^+ channels, the Ca^{2+} sensitive K^+ channels and the ATP-sensitive K^+ channels. Fig. 4.4 illustrates the effect of adding 1 mM of TEA to a population of C6 glioma cells.

The analysis is done in time and frequency domain. In the time traces, fresh C6 cells typically exhibit fluctuations at least in the order of 10 pA. We note that the magnitude of current fluctuations can easily reach 40 pA, viz. after 6 hours without changing the culture medium. This increase in noise has been correlated with changes in extracellular pH level. Fig. 4.4a demonstrates that the signal of freshly deposited adherent C6 glioma cells could be inhibited with the addition of 1 mM of TEA. The inhibitor effect is fast and in less than one minute the current fluctuations switch to less than 2 pA of magnitude. After 50 minutes the cells were washed trice with phosphate buffer saline (PBS) to remove the TEA inhibitor, then fresh culture medium was provided. After washout, the C6 cells slowly regain the original electrical activity as illustrated in the blue curve of fig. 4.4a. The analysis becomes even clearer in the frequency domain. Fig. 4.4b illustrates the current noise spectrum (S_I) of the cells before and after adding TEA. The spectra of the various traces are presented on a double logarithmic scale as a function of frequency. Each spectrum is an average of 25 measurements of 64 seconds. As illustrated in the black curve of fig. 4.4b, fresh C6 cells show a S_I proportional to $1/f^\gamma$, where in most cases $1.5 \leq \gamma \leq 2$. The origin of this dispersion is still under debate. The S_I proportionality can be influenced by the ohmic resistance of the electrolyte between attached membrane and substrate together with the capacitance of the cell-chip contact, or more specifically, by the ion channels in the attached cell membrane that may statistically open and close and generate current fluctuations. After adding TEA, the S_I slowly decays. After 50 min, at 0.1 Hz, the S_I drops nearly 3 orders of magnitude (red curve). The S_I from 60 mHz to 10 Hz becomes flat which is an indicator for thermal noise. After the washout procedure, the S_I is re-established within a timescale of 75 min. The thermal contribution in the spectrum is no longer visible and the S_I follows again the original $1/f^\gamma$ proportionality, where $1.5 \leq \gamma \leq 2$. Thus, our data demonstrate the requirement for K^+ cation flux for the maintenance of electric noise in glioma populations. Yet, given the wide spectrum of TEA inhibitor efficiency, we wished to investigate whether this noise is primarily caused by membrane potential fluctuations, i.e. voltage changes, or other K^+ channel openers, such as extracellular Ca^{2+} ions or ATP. The cross-membrane balance of K^+ ions in all living cells is tightly controlled by the function of the cell membrane-based Na^+/K^+ pump, which maintains inside a cell a comparably high concentration on K^+ ions and a low concentration on Na^+ ions. The opening of voltage-gated K^+ channels

occurs as a response to the decreased membrane potential, generally stimulated by the influx of extracellular Na^+. Thus, we investigated the specific role of voltage-gated Na^+ ion channels in the generation of the electric noise in glioma cells.
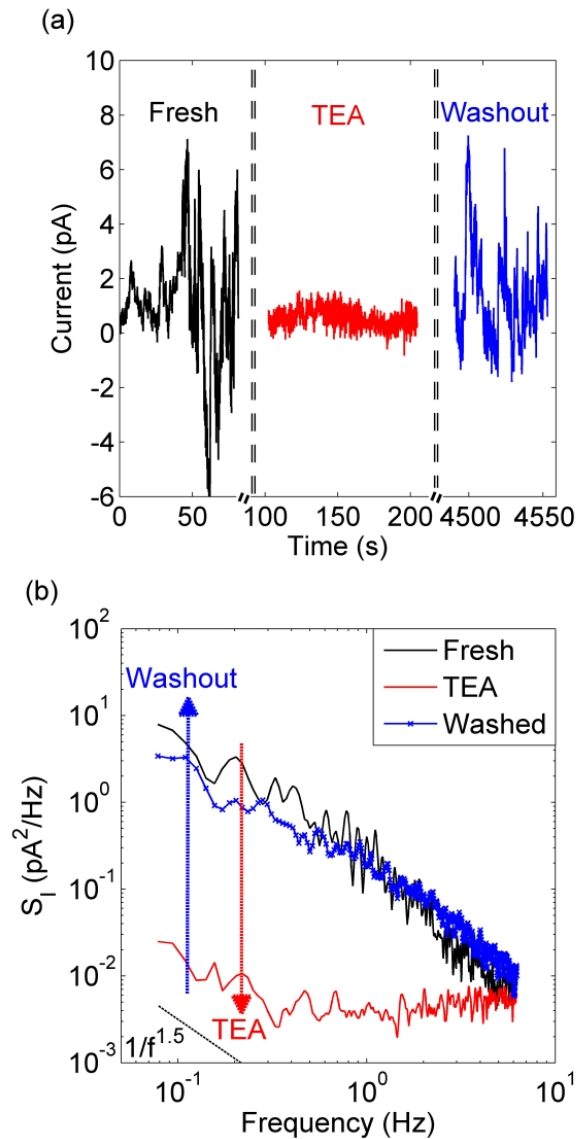

Figure 4.4: Noise blocking influence of 1 mM of TEA in fresh C6 glioma cells (a) In black, the current response during 64 seconds of freshly deposited adherent C6 glioma cells. In red, at 100 seconds, the current response under the influence of 1 mM of TEA is represented. The blue trace represents the current fluctuations after the inhibitor washout process. (b) The current noise spectrum of fresh C6 glioma cells is represented in black. In red, the current noise spectrum is illustrated after adding 1 mM of TEA for 50 minutes. The blue trace represents the current noise spectrum after the inhibitor washout process. Measurement was taken 75 minutes after inhibitor washout. The dashed black curve in the bottom is a guide to the eye representing the proportionality of $1/f^{1.5}$ [1].

Tetrodotoxin (TTX) specifically inhibits the voltage-gated Na^+ channels and does not impinge on the functionality of other various types of Na^+ channels present in glia cells. Fig. 4.5 illustrates the effect of adding 1 µM of TTX to a population of freshly deposited adherent C6 glioma cells. The analysis is presented in both time and frequency domain. The time trace of the freshly adhered cells, prior to inhibition, is represented in Fig. 4.5a (black curve). The red curve represents the signal attenuated with the addition of 1 µM of TTX. The effect is fast and in less than one minute the current fluctuations evolve from a magnitude of about 10 pA to less than 4 pA. After 50 minutes the inhibitor was washed out and fresh culture medium was supplemented. After the washout process, in blue, the C6 cells regain their electrical activity exhibiting similar current magnitudes as in the fresh state. The analysis in the frequency domain is similar to the investigation done with TEA. After adding TTX the current noise spectrum, S_I, at 0.1 Hz drops by 2 orders of magnitude as represented in the red curve of fig. 4.5b. The spectrum reached this stage within 25 min. The noise spectrum from 1 Hz to 10 Hz became flat under the effect of 1 µM TTX, meaning only thermal noise is visible within this frequency range. Some residual activity is still noticeable in the frequency range of 60 mHz to 1 Hz where the S_I spectrum follows a $1/f^{1.5}$ power law. This means that we are not distressing on the functionality of other channels present in the measured cells. After the washout process, the signal slowly comes back until it becomes stable after 90 min, as can be seen by the blue trace of fig. 4.5b. The thermal contribution of the cell noise is no longer visible in the spectrum and the original S_I is re-established. We have established the requirement of the voltage gated Na^+ and K^+ ion channels for the generation of electric noise in glioma cells. Pharmacological inhibition of these channel types ablates the noise efficiently, but does not affect the cell viability or the long-term electrophysiology. After the inhibitors were washed out, glioma cells were able to recover in a short time. Their electric noise activity was then fully restored to the levels observed prior to inhibition.

Concluding, we have demonstrated that electrical current noise of glioma C6 glioma cells is dominated by the flow of Na^+ and K^+ ions through their respective voltage-gated channels. The electrical activity can be effectively abolished using specific pharmacological inhibitors. Given the technical setup of measuring several hundreds of thousands cells as a single population, we presume that these oscillations must be happening in a concerted and likely a functional pattern, at least across a sufficient number of cells at the same time, to become detectable. Thus, individually electrically active glioma cells can coordinate continuous and diverse electric responses in the picoampere-range throughout large cell populations. Our transducer therefore allows detection and precise measurements of such electric activities of large cancer cell populations and may be used as reference for studying overall electrophysiological properties of tumor bulks *in vivo* [1].
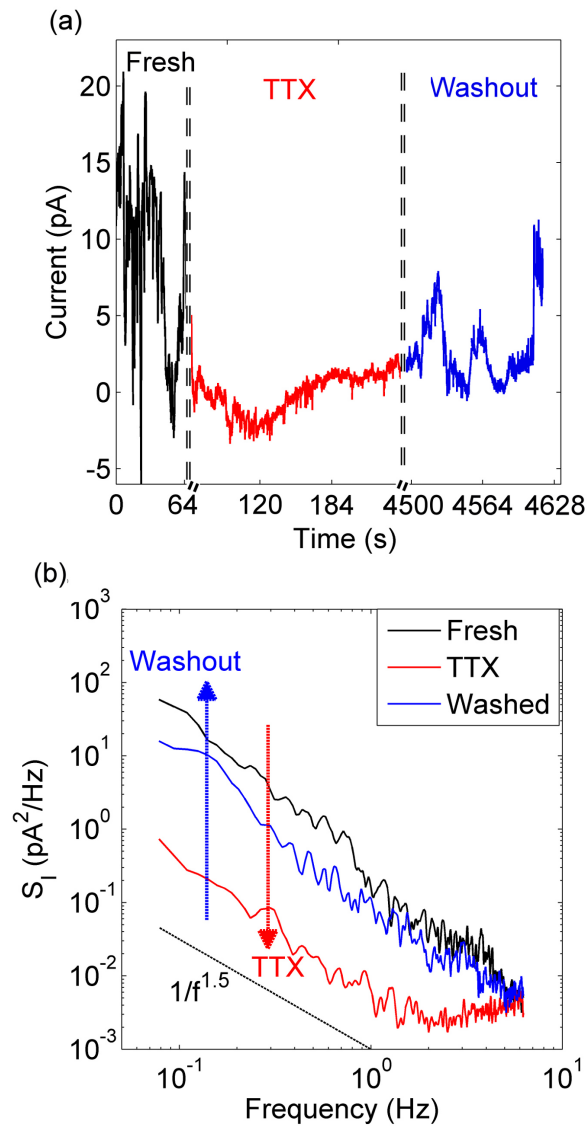
Figure 4.5: Noise blocking influence of 1 µM of TTX in fresh C6 glioma cells (a) In black, the current response during 64 seconds of freshly deposited adherent C6 glioma cells. In red, at about 100 seconds, the current response under the influence of 1 µM of TTX is represented. The blue trace represents the current fluctuations after the inhibitor washout process. (b) The current noise spectrum of fresh C6 glioma cells is represented in black. In red, the current noise spectrum is illustrated after adding 1 µM of TTX for 50 minutes. The blue trace represents the current noise spectrum after the inhibitor washout process. Measurement was taken 90 minutes after inhibitor washout. The dashed black curve in the bottom is a guide to the eye representing the proportionality of $1/f^{1.5}$ [1].

4.3 Maturing of primary neurons: neuronal network formation

In the previous sections, we presented biolelectronic activity in glioma cell populations. With these experiments, we were able to validate our system. Our setup is suitable for such measurements of bioelectronic activity within *in vitro* cell populations. Moreover, we investigated the source of the obtained current signals, which we consider to originate mainly from potassium and sodium ionic currents through ion channels in the cell membrane [1].

Here, we now present the long-term monitoring of bioelectronic activity of a neuron population *in vitro*. For this experiment, a murine, embryonic hippocampal neuron population of 400.000 cells was seeded on a new in-house transducer. The current signal was continuously recorded for a duration of about 2 weeks. The recording was started on 3rd day *in vitro*. The purpose of this experiment was the monitoring of bioelectronic activity of these young, fresh neurons forming a neuronal network on the transducer. We were interested in the detection of characteristic indicators within the current signal, that might be related to neuronal network formation as well as neuronal network communication. Therefore, we present the detailed analysis of some specific signals with the method of spectrogram in the next section.

In fig. 4.6 we depict the result of the long-term current recording of a neuron population with the in-house transducer for about 205 hours as an overview. For this plot, bioelectronic signals obtained from the measurement were appended in time, yet interrupts in the recording are not shown. The measurement was mostly performed with the 0.1 cm^2 electrodes. In general, the new transducers yield a significant higher current magnitude compared to the Philips chips. We consider the larger electrode size to mainly determine the transducer's increased sensitivity. In addition, more neurons contribute to the overall electric current level on a bigger electrode area.

The signal in fig. 4.6 demonstrates the evolution of bioelectronic activity of the neuron population. In the first 20 hours, the signal is relatively weak around 2 nA. It evolves to higher magnitudes with time, up to 50 nA between 20 and 60 hours. Beyond 70 hours in time, the magnitude of the signal increases significantly, and the low frequent current fluctuations reach roughly 1000 nA around 120 to 160 hours. Also a huge current offset oscillation can be observed between 80 and 200 hours. The quality of the current signal evolves during the measurement. The signal fluctuations show a huge variety. Details will be discussed in the following.
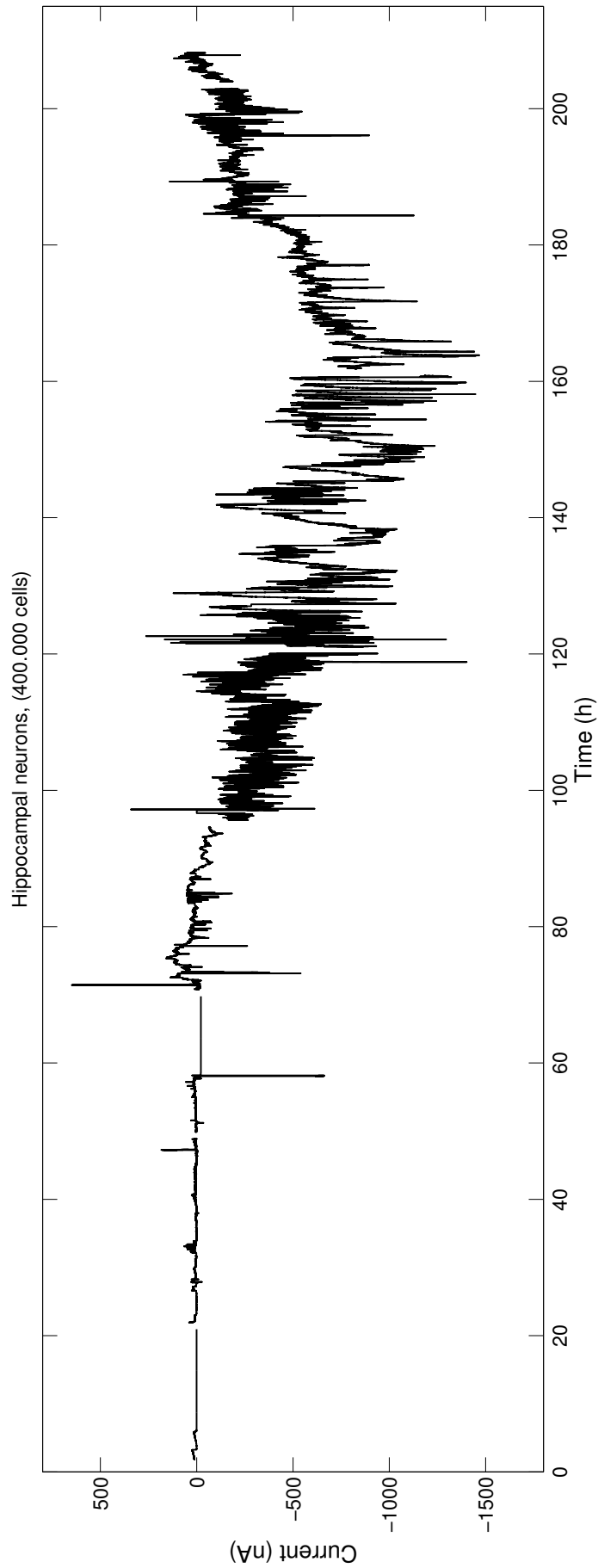
Figure 4.6: Overview of the long-term recording of a murine, hippocampal neuron population with the in-house transducer for about 200 hours. The bioelectronic activity evolves with time and shows a huge diversity in current fluctuations.

4.3.1 Spectrogram tool for analysis of bioelectronic activity

The stationary spectral analysis of recorded signals from cells is useful to analyze the power spectral density distribution within a signal as described in section 1.2.2. This method gives a good overview of the contained frequencies, but it comes to its limits when analyzing a long time signal, as single spectral events are not clearly visible. This is due to the analysis' nature as it calculates only one PSD for a signal. Temporary occurring events like fast spiking get buried in the averaged PSD, because they are limited in time and therefore not significant in the spectrum.

Based on the PSD analysis in section 1.2.4, we now present a novel method to analyze the spectral evolution of a bioelectronic signal, especially in the long-term recording of the neuron population in this chapter. To obtain a time-resolved spectral analysis, in principle, the long-term current signal is subsequently analyzed and appended in time. Therefore, the *full* signal is sliced into several windows, which are then subsequently fed to the `pwelch` algorithm presented in s section 1.2.2.

The software for the time-resolved spectral analysis outputs a matrix, that contains the data for the particular time, the frequencies and the calculated PSD magnitudes for each signal slice. A common representation of a time-resolved PSD analysis $S_I(f, t)$ by means of a 3D visualization is called *spectrogram*.

The time resolution and the spectral resolution of the obtained spectrogram can neither be accurate at once, as they are limited by fundamentals in physics respectively in signal theory. Based on *Heisenberg's principle of indeterminacy* with contributions of *W. Pauli* [13], the relation between the uncertainties in time Δt and in frequency Δf can be generally stated as

$$\Delta t \cdot \Delta f \simeq 1 \quad . \tag{4.1}$$

This identity states that the time t and the frequency f cannot be simultaneously defined in an exact way. Hence, the user has to consider this limitation of accuracy when operating the spectrogram analysis.

The time resolution of the spectrogram is mainly determined by the duration of the signal segments, that are passed to the `pwelch` algorithm. Assuming a short interval, for example 2 seconds, the spectrogram algorithm will calculate a PSD every 2 seconds and thus feature a relatively high resolution in time. Consequently, the spectral resolution is reduced accordingly. Vice versa, if a high spectral resolution is required for e.g. detection of particular frequencies, the time resolution will be decreased due to longer time intervals.

Figure 4.7 depicts such an output of the spectrogram software in MATLAB, where we show a *spectrogram* obtained from the aforementioned hippocampal neuron measurement. The interval of the analyzed current signal is shown below the spectrogram in fig. 4.7. In the spectrogram, the x-axis represents the time of analysis relating to the signal, while the y-axis shows the frequency range. The z-axis displays the values $S_I(f)$ of the obtained PSD curves for each signal slice. For better visualization, the magnitudes of the spectra were plotted as a surface and color-coded according to the colorbar on the right.

We here introduce the method of *spectrogram* as a basis for the following analysis. For the comparative analysis of the obtained bioelectronic signals from the neurons in the previous section, we do not use the spectrogram in 3D visualization as shown in fig 4.7. For clarity, we employ a top view to only visualize the time-frequency plane in the following. With this method, the spectral evolution of the recorded signals can be monitored and explored. The accuracy in time and frequency respectively depends on the selected parameters like time intervals of the analysis.
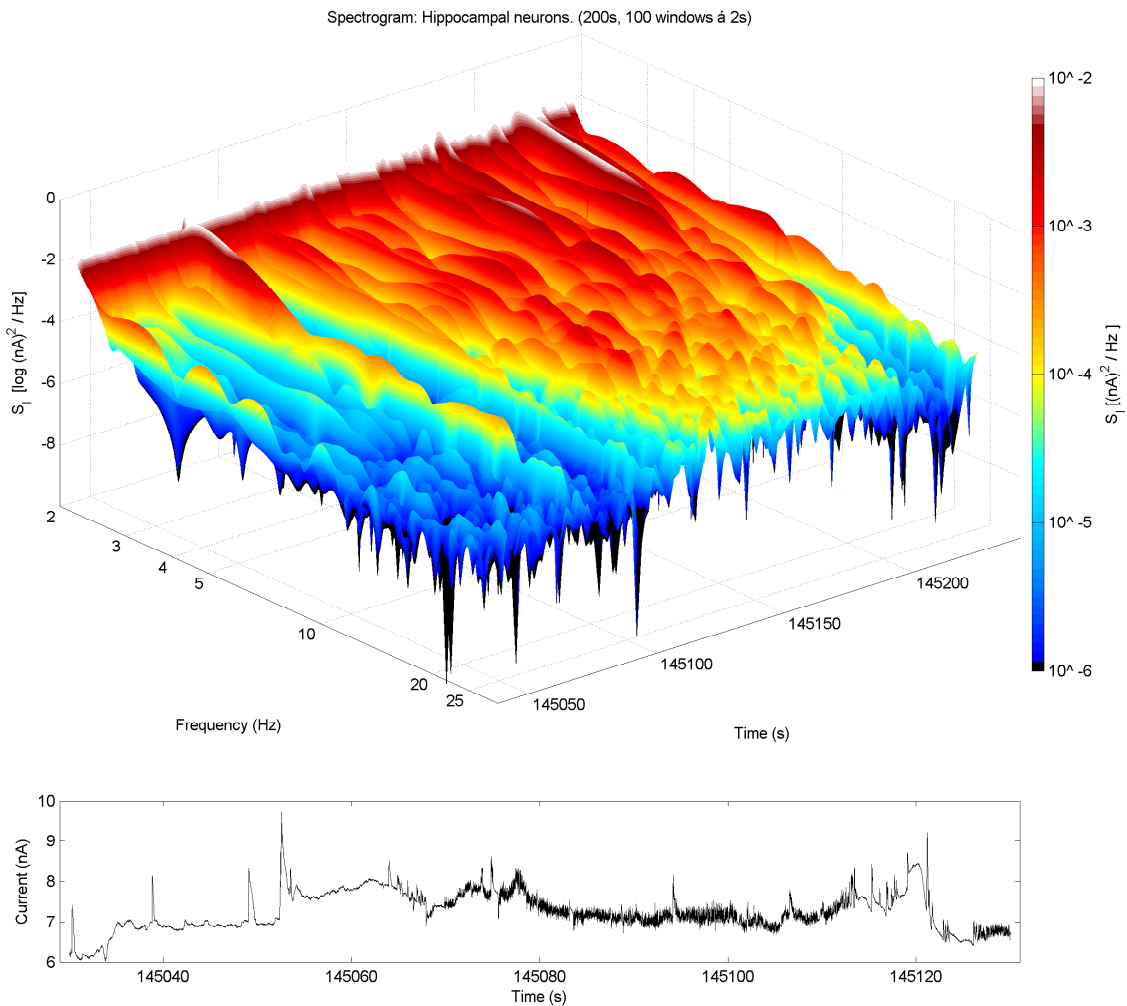

Figure 4.7: Example of time-resolved spectral analysis, the spectrogram, obtained from the current signal below. The PSD spectra of individually analyzed time intervals of the signal are appended in time and represented in a 3D visualization. The magnitude of the PSD spectra was color-coded according to the colorbar.

4.3.2 Bioelectronic activity in neuronal networks

In the following we show different examples of the recorded bioelectronic activity of the neuron population in the previous section. This long-term measurement was performed for about 200 hours, why we expose a selection of interesting intervals of bioelectronic activity. Moreover, we also demonstrate the capability of the spectrogram software to reveal hidden spectral events within the signals.

The samples of the current signals presented in the following state the evolution of bioelectronic activity within the neuron population. The signals were extracted in a chronological order, starting at the beginning of the measurement, which was day 3 *in vitro*. In this section, we present the existence of neuronal network formation both in the current signals and in microscopic images. Hence, we demonstrate the suitability of our system to investigate populations of neurons over a long time.

At the beginning of the measuring period of the neuron population, a control batch was observed in an optical microscope. This batch contained less neurons, roughly 250.000, compared to the measured batch, which comprised 400.000 neurons. However, the control batch was suitable for demonstration of the initial state of the neurons on the transducer. Fig. 4.8 shows four different magnifications of the neuron population on top of the transducing electrodes. In fig. 4.8a, a part of the $0.1\,cm^2$ area electrode is visible. The small dots on top of the electrode are the neurons adherent to the transducer surface on day 2 *in vitro*. They are nearly equally distributed over the transducer. In fig. 4.8b and c) the emerging neurons can be observed in higher detail. They are in an embryonic state and do not exhibit a strong interconnectivity yet. Some neurons have already formed axons and dendrites, with which they established sporadic connections to other cells. In general, the neurons exist mostly separated from each other. Fig. 4.8d is a high magnification on a small number of neurons. Here the inter-neuronal connections can be observed in an initiating state. The number of neuronal connections, formed by axons and dendrites between the neurons, at this early state is remarkable. This figure depicts the beginning of *in vitro* neuronal network formation in our transducer.

In the microscopic images in fig. 4.8, we found the neurons to exist mostly separated from each other. Therefore, we expect the neurons to act in a way related to single cell behavior regarding their biolelectronic activity. In fig. 4.9, we show an example of the recorded signals in this early state of the neurons. Here we present a current signal of 60 seconds duration, which was extracted about 2 hours after the measurement was started on 3rd day *in vitro*. Below the current signal in nA, we show the obtained spectrogram analysis described in section 4.3.1, where we solely represent the time-frequency plane. The time scale in seconds on the x-axis is valid for both the current and spectrogram plot. The following examples of selected signals are represented identically.

In general, the interpretation and understanding of the recorded bioelectronic activity is complex and difficult, why we here may present a first estimate of the signal's origins.
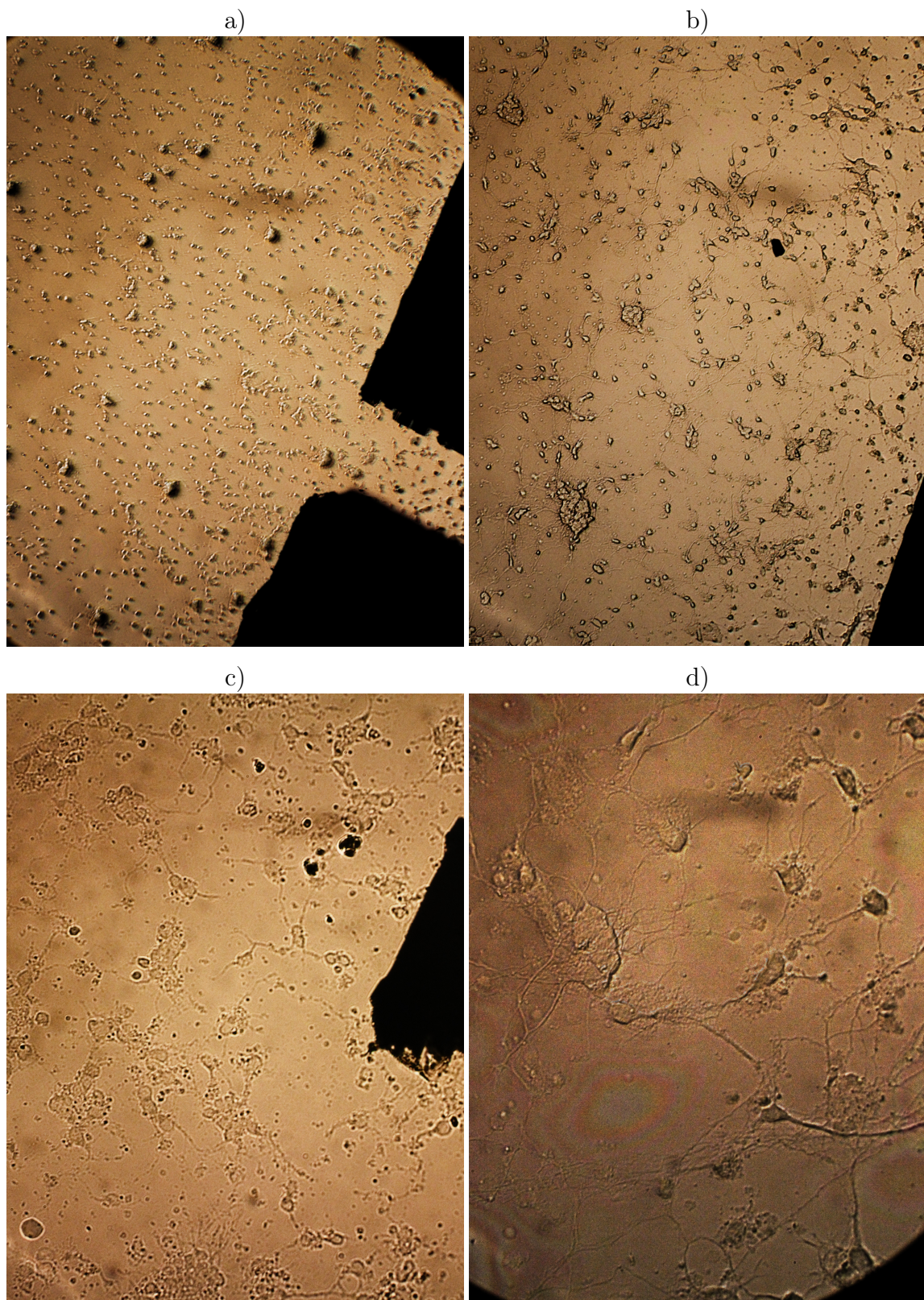
Figure 4.8: Microscopic images of different magnification of the fresh neuron population (day 2 *in vitro*) attached on the 0.1 cm^2 electrode on our transducer. This control batch included about 250.000 neurons. a) Gold electrode with several neurons distributed equally over the surface. b) Magnification of the electrode. Neurons are mostly separated. Some agglomerates are visible. Some neurons did already form axons and dendrites. c) In between some neurons, connections have already been established. d) High magnification of neurons forming synaptic connections and hence start the formation of a neuronal network.

The current signal in fig. 4.9 shows a low frequent fluctuation of about 1.5 nA, which is relatively low. Within the signal, faster oscillations can be observed. They happen randomly in an uncoordinated manner and seem to occur spontaneously. The magnitudes of this current noise is roughly 0.5 nA. Regarding the spectral analysis, these fast oscillations in the range of 1 to 10 Hz exhibit spectral magnitudes around $10^{-4}...10^{-2}$ (nA)^2/Hz. The selected signal is representative for the bioelectronic behavior of the neurons in the first hours of the measurement. The current signal is quiet noisy. With reference to the microscope images in fig. 4.8, we consider the recorded current signals to be typical of rather separated neurons with a low level of interconnectivity. Therefore, we relate this example to *single cell behavior*, which is rather uncoordinated and spontaneous, asynchronous and low in magnitude.
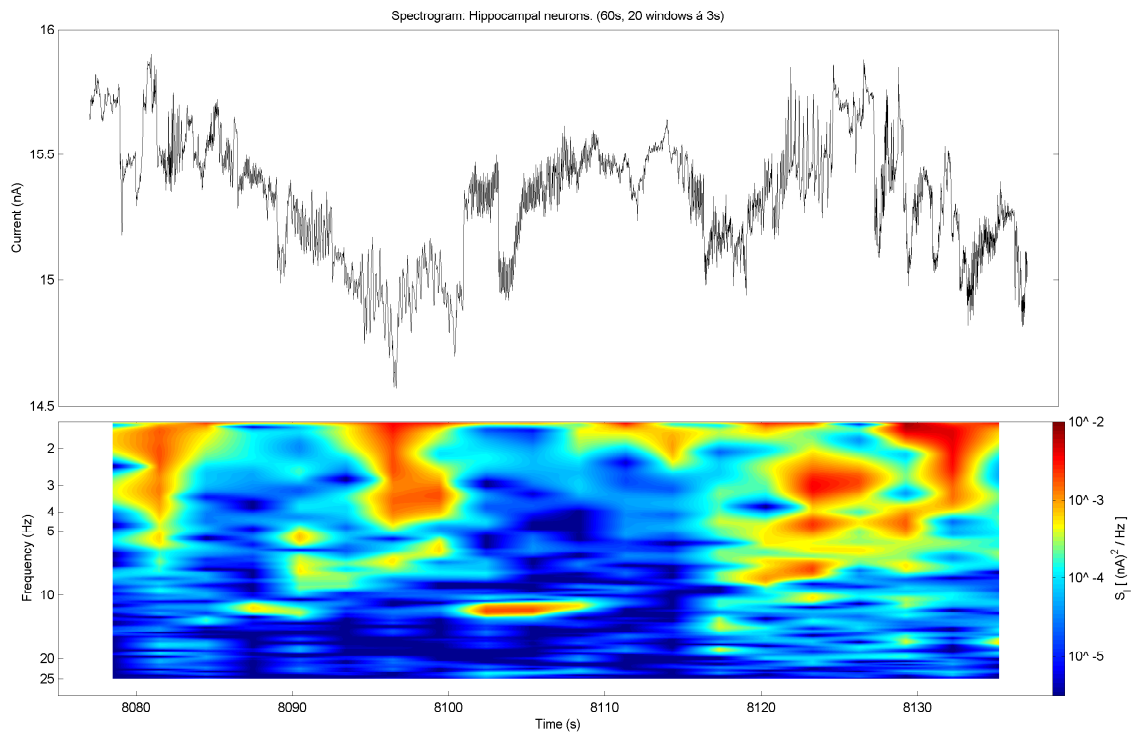
Figure 4.9: Analysis of bioelectronic activity both in current time course and spectrogram of a signal from the beginning of the measurement. The bioelectronic activity shown an uncoordinated, spontaneous and asynchronous behavior, which is associated with single cell behavior.

In fig. 4.10, we exemplify a current signal of 200 seconds duration, which was recorded after roughly 40 hours. In this signal, we observe a different bioelectronic behavior compared to fig. 4.9. Firstly, the shape of the signal changes. In the first half, the signal shows low frequent current oscillations which increased up to 4 nA, while the current noise is relatively low. The current noise decreased to roughly 50 pA. Moreover, current peaks are visible. We consider these events in the signal to feature a higher level of coordination compared to fresh neurons. If we consider the random current noise of the signals to originate from rather statistical ion currents, as described in section 1.2.3, we assume that such visible peaks in the current signals result from a collaborative network activity within the neurons. If such a bioelectronic event was caused by only one neuron for example, we expect the according magnitude to be minute, or rather invisible in this type of measurement. In the second half of the signal, a period of fast fluctuations can be observed. It occurs in a spontaneous manner and lasts about 60 seconds. In the spectrogram, the period of these fast current oscillations is clearly visible in frequencies up to 20 Hz. With the spectrogram analysis, such regions of fast oscillation can be easily detected. Summarizing, this example features a beginning collaborative network activity in combination with spontaneous random bioelectronic activity.
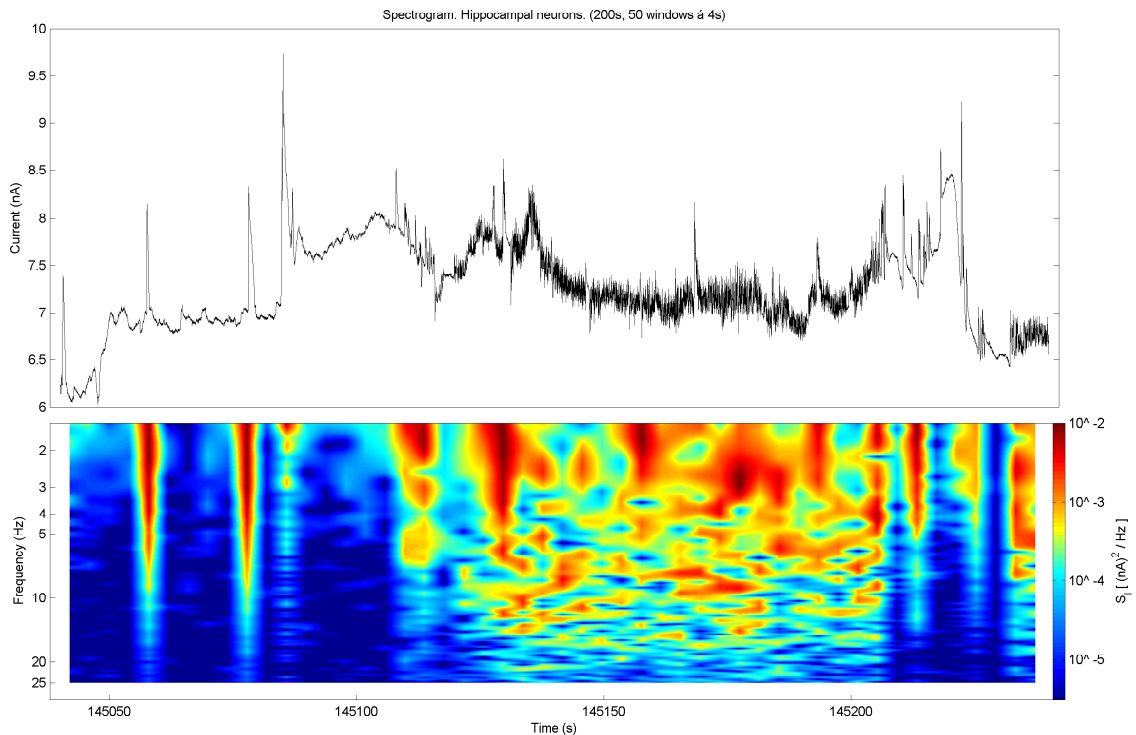

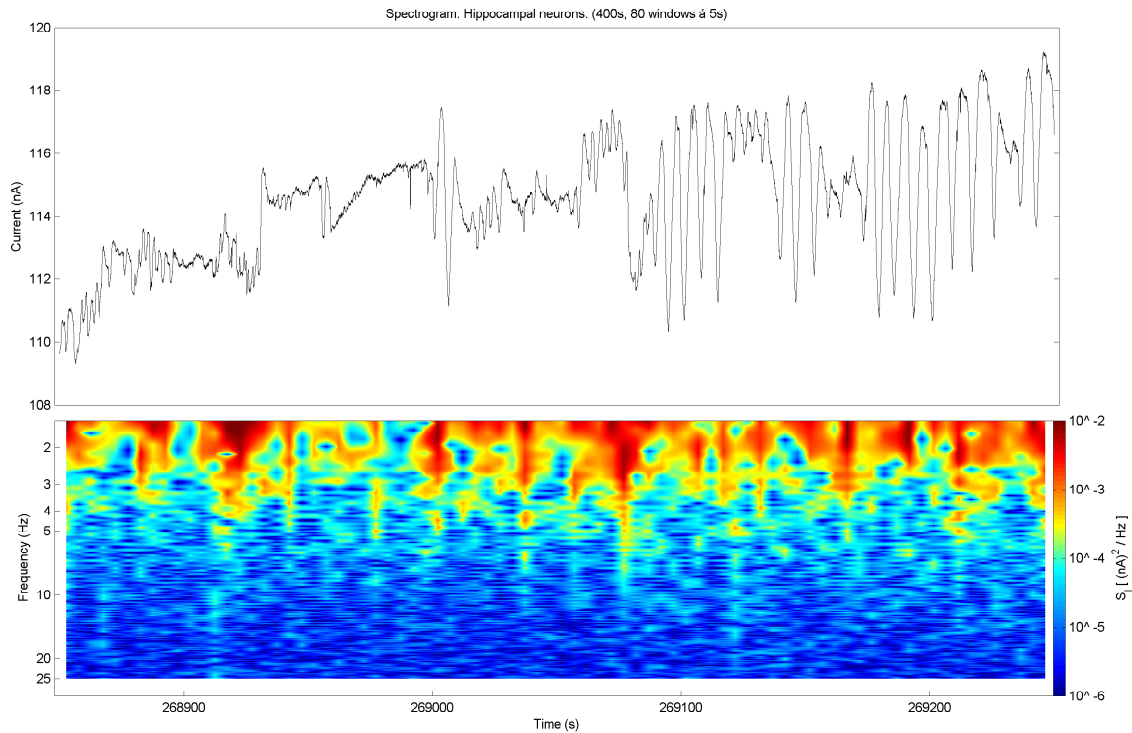**Figure 4.10:** Analysis of bioelectronic activity both in current time course and spectrogram of a signal after 40 hours, that shows a beginning collaborative network activity in combination with spontaneous random bioelectronic activity. Spontaneously occurring fast current fluctuations can be detected by the spectrogram analysis.

The neuron population evolves with time to form a neuronal network, which exhibits a high level of network communication due to well established neuronal connections. In fig. 4.11, a 'midway' current signal of 400 seconds duration is presented, which was recorded after 72 hours. Here, we observe a high amount of low frequent current fluctuations up to 8 nA rather than fast oscillations. These low frequent periodic events are visible in the second half of the signal and range in the frequency below 5 Hz. The curve is relatively smooth, which gets confirmed by the spectrogram: The major fraction of the spectral magnitude is located below 4...5 Hz within the whole signal. Low frequent periodic and coordinated patterns can be observed within many regions in the signals in this state of the neurons. We consider these patterns to be highly functional and biologically relevant.

Figure 4.11: Analysis of bioelectronic activity both in current time course and spectrogram of a signal after 72 hours. Coordinated and synchronous low frequent oscillations exhibit a decent level of network communication within the neuronal network and are expected to be highly functional.

Another example of neuronal network behavior is shown in fig. 4.12, which was recorded after 87 hours. We observe a coordinated network activity, since the current signal features a long lasting, periodic and synchronous bioelectronic activity. These slow oscillations with magnitude of 3 nA are related to synchronous, collaborative electric activity of the neurons, which have now established a decent level of interconnectivity. They feature a constant intensity over a wide range of time, but are not considered to relate to action potentials. In comparison to previous examples, the magnitude of these wavelike structures is relatively low. Moreover, the amount of fast fluctuations is almost negligible.

The spectrogram confirms that most of the spectral magnitude, which is related to the signals energy, is contained in these slow oscillations in the range below 5 Hz. In addition, a continuous band of spectral activity can be observed around 7...8 Hz, which is not obvious to detect by eye in the signal. In a more detailed representation, the origin of this spectral component can be found in fast, weak periodic patterns which overlay with the low frequent oscillations. These additional patterns are represented in the inset in fig. 4.12, where a magnification of one low frequent oscillation is depicted. The period of these fast patterns corresponds to the observed frequency band in the spectrogram. This is one example of the ability to detect particular bioelectronic activity within a long-term signal by means of the spectrogram software.
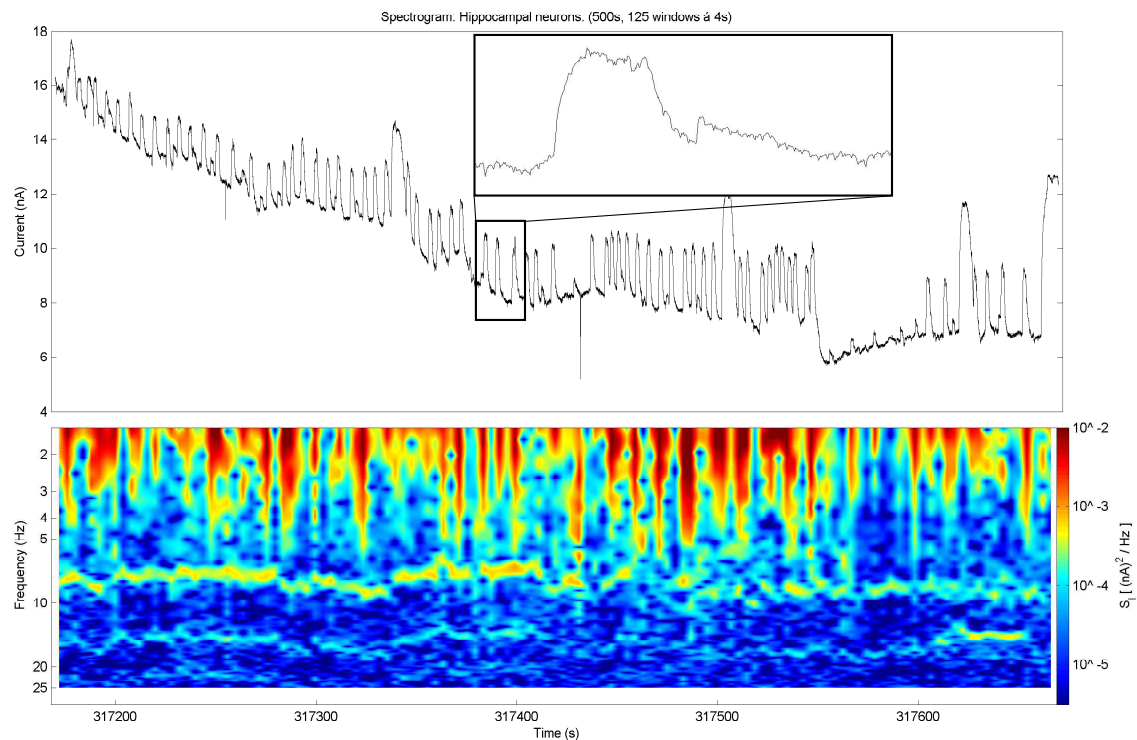

Figure 4.12: Analysis of bioelectronic activity both in current time course and spectrogram of a signal after 87 hours. Long-lasting, periodic wavelike patterns can be observed, that relate to a high level of neuronal interconnectivity. The spectrogram reveals faster patterns within the signal, shown in the inset.

A different example for coordinated, synchronous and rhythmic bioelectronic activity within the neuronal network is given in fig. 4.13, recorded after 100 hours. Again, the current signal shows very slow current oscillations with magnitudes up to 150 nA, which is huge compared to the beginning of the measurement. The existence of these huge current waves, observed also in fig. 4.11 and 4.12, exemplifies the large variety of such biologically relevant processes. The high magnitudes contained in the current signal due to the low frequent oscillations can also be observed in the spectrogram, where they exhibit spectral magnitudes beyond 10^0 (nA)^2/Hz. The neuronal network now features significantly higher bioelectronic activity at this maturity, compared to the beginning of the experiment. Hence, the color scale of the spectrogram was adapted to higher magnitudes for proper representation.

Similar to the signal in fig. 4.12, a band of spectral activity can be observed mainly in the frequency range around 4 Hz. The inset in fig. 4.13 reveals again rhythmic current pattern to be the origin. At the end of the signal, the spectrogram shows one frequency band moving towards lower frequency with time. Here, the duration of the overlaying patterns increases accordingly. Such spectral evolution can be detected and investigated with this method.
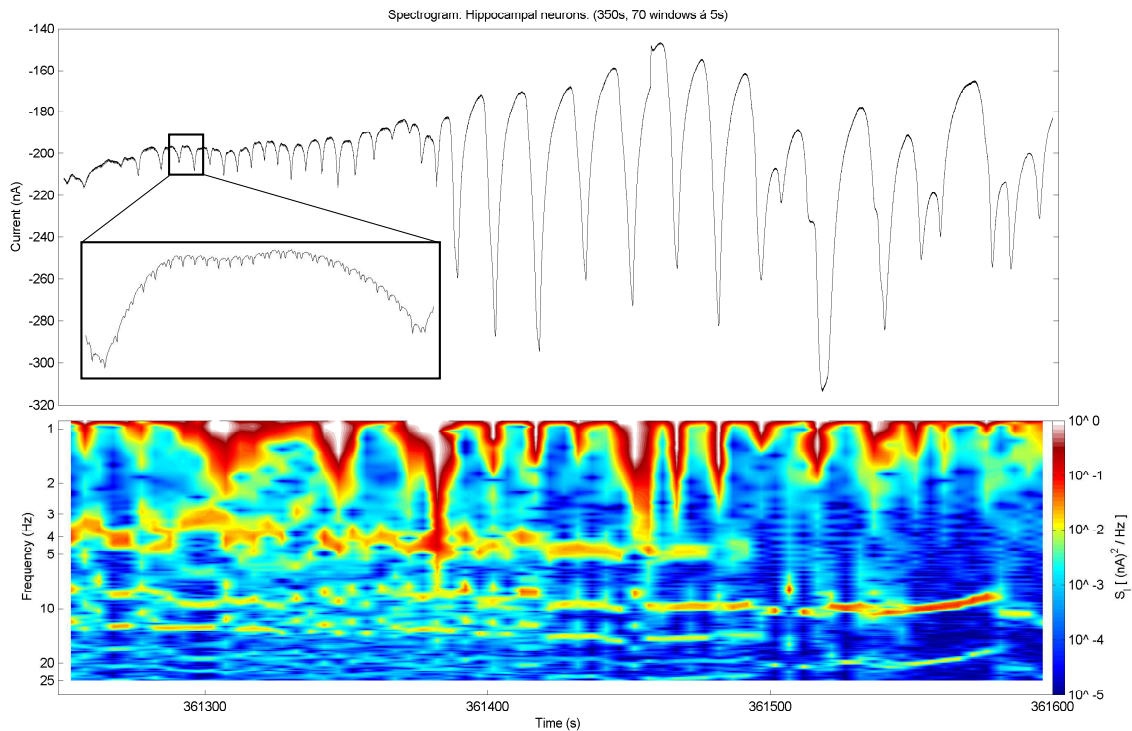

Figure 4.13: Analysis of bioelectronic activity both in current time course and spectrogram of a signal after 100 hours. Very slow current oscillations with large magnitude of 150 nA are observable. With the spectrogram, fast current fluctuations on top of the wavelike structures are revealed. Such pronounced bioelectronic activity depicts the well established neuronal network activity and communication.

Finally, we present an example from the end of the measuring period. A current signal of a mature neuronal network of 1000 seconds duration was recorded after 204 hours and is shown in fig. 4.14. In this signal, we find numerous incidents of different bioelectronic events. The signal exhibits slow events like for example current fluctuations around 80 nA and regions of huge current plateaus. Moreover, in consistency with the spectrogram analysis, the signal is thoroughly composed of faster peaks or waves, which are depicted in the inset. These relatively fast events are the origin of the decent spectral activity in the range of 1...10 Hz. The magnitude of these waves is roughly 10 nA, which is remarkable.
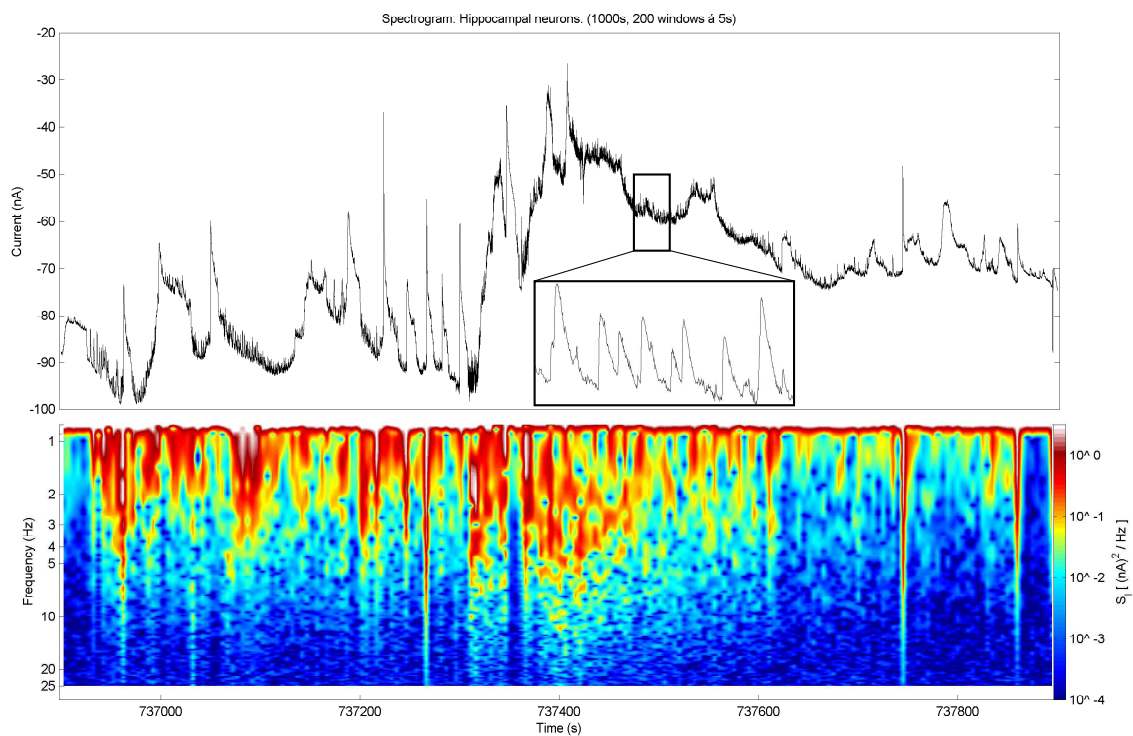
Figure 4.14: Analysis of bioelectronic activity both in current time course and spectrogram of a signal at the end of the recording period. Numerous incidents of bioelectronic events show the complex network activity. The signal is composed of huge current fluctuations that contain wavelike structures (inset), current plateaus and spikes. The complexity of the current signals is remarkable at this maturity of the neuronal network.

The recorded current signals at the end of the experiment differ significantly from the signals obtained at the beginning. The fast current fluctuations, which we termed current noise are considered to originate from random, spontaneous ionic currents across the cell membranes of the neurons. The magnitude of the current noise decreased within the measuring period and could be found only sporadically in the signals at the end of the experiment. Within the recorded signals, we found numerous regions which feature low frequent current oscillations, that were mostly periodic and of huge magnitudes. With time, the magnitude of these intensely pronounced patterns even increased. We assume that these low frequent waves result from a collaborative,simultaneous and synchronous bioelectronic activity of an enormous number of neurons in the transducer. For establishing such a high degree of collaborative behavior, the neurons have to connect to each other and build up a neuronal network communication. This communication is supposed to happen via inter-neuronal connections. We observed the evolution of bioelectronic signals from an isolated *single cell behavior* towards a neuronal network communication. Based on the obtained current signals, we therefore state the existence of *in vitro* neuronal network formation inside our transducer.

As an evidence for neuronal network formation, the measured transducer was inspected with optical microscopy at the end of the experiment, which is shown in fig. 4.15. In fact, the degree of neuronal network formation is remarkable. The young embryonic neurons established a (or more) highly connected neuronal networks and colonized on top of the transducer. Fig. 4.15a shows the 0.1 cm^2 electrode, which is covered with large agglomerates of neurons. These neuron bulks are connected to neighboring bulks by 'roads' of neurons including their cellular extensions. Fig. 4.15b,c show magnifications of these neuron bulks. The cell bodies and the interneuronal connections are visible. Particularly in fig. 4.15c the complexity of such neuronal networks becomes apparent. The observed bioelectronic activity in the current recordings is expected to happen within these networks, by means ob collaborative biological activity of several hundred or thousands of neurons on the gold electrodes.
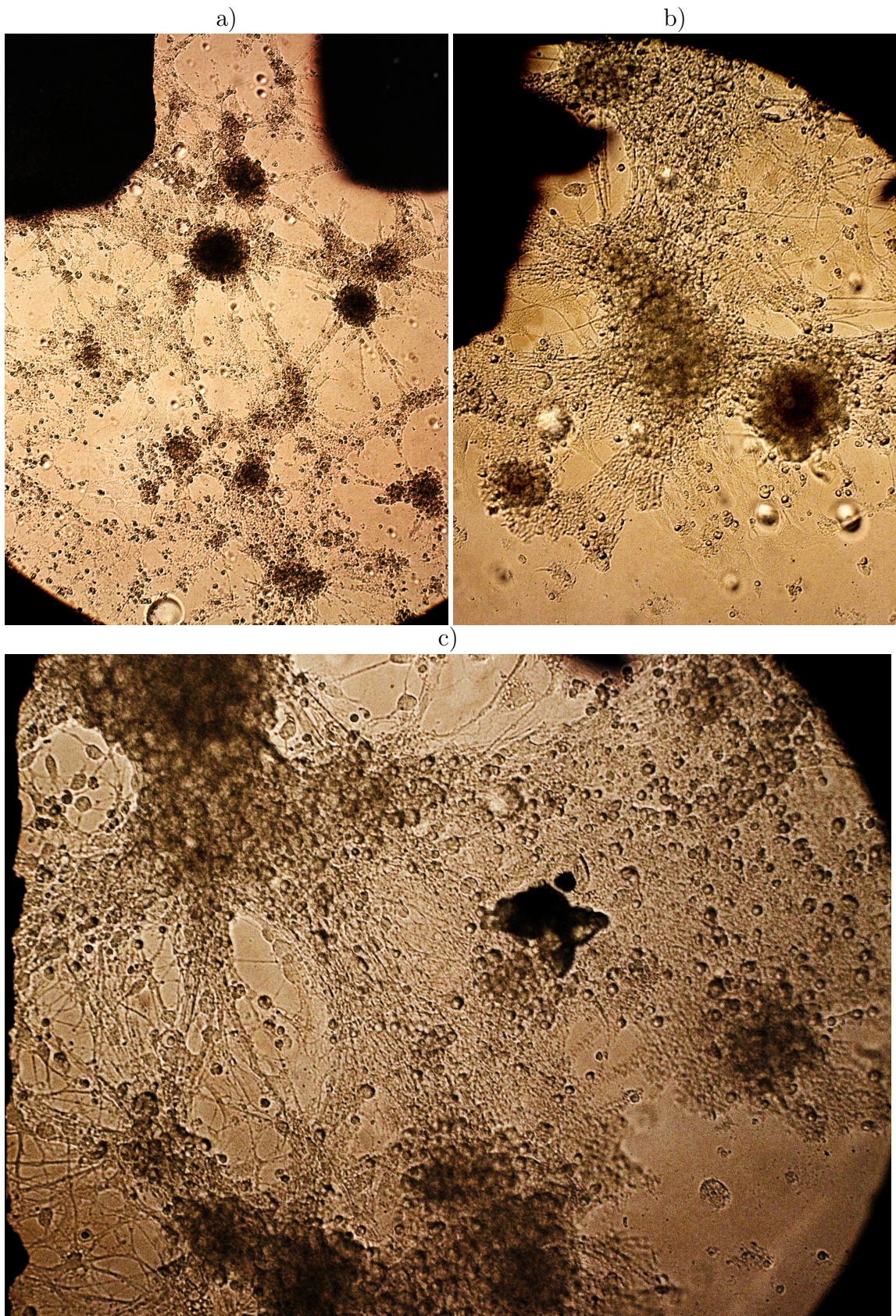
a) b)

c)

Figure 4.15: Microscopic images of the transducer after the measuring period. The embryonic neurons have established a complex network, with thousands of cells included. They form a high degree of connectivity in between huge bulks (a). The magnifications of these bulks emphasizes the complexity of such neuronal networks (b,c).

5 Future work

The experimental setup, which we presented in this work, allowed us to accurately record different current signals from cell populations *in vitro*. We performed experiments on populations of C6 glioma cells with a commercial sensing device. Thus, we identified the obtained current signals to originate from ion channels in the cell membranes. Moreover, we developed and manufactured in-house transducers, that were used to successfully record current signals from a primary neuron population over almost 2 weeks. Here, we observed the formation of neuronal networks, why the evolution of bioelectronic activity in the obtained signals was associated to neuronal network communication. This long-term experiment was the first measurement of a cell population performed with the new transducers.

In the future, we will focus on both the technical improvement of our setup and performing measurements of different cells.
Regarding the equipment, we started experiments on the electrical characterization of the transducers to obtain profound knowledge on the parameters, that dictate the electrical properties of the transducer. Therefore, we will perform deeper electrical studies by means of impedance spectroscopy and current noise analysis to learn about the influence of parameters like electrode size, electrode thickness and roughness, electrode geometry, ionic concentration of the electrolyte and so on. The purpose of such electrical characterization is also to continuously improve the equivalent circuit models by extraction of parameters like charge transfer resistance or the dispersive CPE exponent. However, such studies are extensive and complicated. Ultimately, they will help to find an optimal transducer design for capacitive current recordings of cell populations *in vitro*.

Moreover, we are interested in the correlation between current and voltage measurements of bioelectronic activity. So far, we obtained preliminary results from experiments, where the electrical activity of cells was recorded simultaneously in current and voltage within one transducer. The correlation of extracellular potentials and currents is not obvious to understand, why such studies are currently of high interest.

In the near future, we will also work on technical improvement of different components, such as for example the device holder. The sealing between the glued PMMA lid and the glass substrate leaked from time to time. The idea here is to develop an integrated design of the holder, meaning the absence of the compartment. The new

holder will feature an integrated well for the culture medium, which forms a tight seal with the substrate and is therefore also suitable for sterilization.

In general, the technical equipment will be continuously improved and adapted to the particular purpose.

Regarding the long-term recording of neuron populations, we will focus on developing a database of bioelectronic signals of neuronal networks. Therefore, we will perform multiple measurements similar to the results presented in section 4.3, but with different genotypes of neurons. The purpose is to obtain an overview of different bioelectronic behavior regarding for example the overall activity or excitability of a particular genotype.

In addition to merely long-time recording of bioelectronic activity, we are interested in the investigation of particular biologically relevant events regarding a neuronal network. In our work, we will focus on the *learning and memory* within neuronal networks *in vitro*. Studies in neuroscience report the formation of memory related to synaptic activation of the neurons, called long-term potentiation (LTP). The different effect, synaptic depression is called long-term depression (LTD) [14] [15] [16] [17]. These mechanisms are considered to play a major role in memory formation and degradation in the brain, which is termed neuronal plasticity. Moreover, these effects can be evoked by means of electrical stimulation with pulses or pulse trains [18] [19].

Preliminary experiments on this issue were performed during this work. Therefore, fast pulse bursts in the 1kHz range were non-invasively applied to the neuronal network and the response was recorded. After such fast stimulation, which is considered to evoke LTP, where the bioelectonic activity of the neuronal network increases, we observed a significant increase of the current magnitudes during the following hours. This experiment was repeated with different neuron populations and could be reproduced.

Another method for the modification of bioelectronic activity within neuronal networks is the usage of chemical agents. A first example was presented in section 4.2 and [1], where we used ion channel inhibitors, TEA and TTX, that block specific ion channels and therefore manipulate the electric activity of the cells. In contrast, we added small quantities of the neurotransmitter-like acting drug Lysophosphatidic acid (LPA). This resulted in a fast increase of the current magnitude within seconds and minutes.

Summarizing, by means of electrical stimulation with pulse trains and chemical stimulation, there are tools available to study the network behavior under the influence of such parameters. Therefore, experiments on the effects of such stimuli on the neuronal network communication will be performed. In the future, this may help to understand relevant medical issues like for example the biological processes in the brain caused by anesthetics during surgery.

Lastly, we are also working on the *in vitro* learning of neuronal networks, which seems to be a novel sector in bioelectronics and medicine. The goal is to teach a neuronal network for example a particular pulse train, which is autonomously repeated by the neuronal network, even without stimulation. Preliminary experiments have been performed in the recent past. The results are promising, since we did succeed to – very simplified – teach a neuronal network to autonomously repeat an external signal for a long time. The field of *in vitro* learning and memory formation is of major interest for neuroscience and will for sure be one of the big questions to study in the future.

6 Conclusion

In this work, we focused on low-frequent electric current measurements of cell populations *in vitro*. Therefore, a low-noise measuring system was developed, which allowed us to detect and acquire minute capacitive membrane current fluctuations across large populations of brain cells in the picoampere range. We studied the bioelectronic activity within C6 glioma cells and primary hippocampal neurons *in vitro*.

The experimental setup for recording bioelectronic activity of cell populations can be divided in four different segments: A transducer, which holds the cells and the culture medium, the peripheral highly sensitive measuring equipment, the data acquisition unit and a customized design and arrangement of all components to achieve an ultra low-level detection limit.

In the beginning, we used a commercial transducer and recently started the in-house fabrication of newly developed transducers. The developed transducers feature thin gold electrodes of different area on glass substrates, to also study different electrical properties of the metal-electrolyte interface, which is the junction site between electrodes in contact with the culture medium. For equivalent circuit modeling, we use a modified Double RC circuit, that includes a dispersive constant phase element. Hence, we were able to model the realistic impedance and capacitance behavior of the transducers in good agreement with measured data obtained from impedance spectroscopy.

For a measurement, the transducer with the cells was mounted inside a modified incubator to provide an ideal physiological atmosphere for the cell maintenance. The adjacent peripheral measuring equipment comprises mainly a low-noise current preamplifier and dynamic signal analyzer. The transducer is connected to the preamplifier and the measured current signals are digitalized with high accuracy. The data is transferred from the analyzer to a computer by an acquisition software written in LabVIEW, which allows the fully remote controlled operation of the long-term measurements.

For reducing parasitic impacts like interfering signals from power lines etc., the measuring equipment was encased in a large Faraday's cage for electromagnetic shielding. Moreover, low-noise cables were thoroughly used for any sensitive electrical connection.

With this novel method we present a state-of-the-art yet simple approach for the long-term monitoring of bioelectonic activity of cell populations *in vitro*.
We have demonstrated that our sensing system allows non-invasive detection of electrical activity of large cell populations of even electrically quiescent and non-excitable HeLa cells, that exceeds the system's intrinsic detection limit of 0.5 pA.

Experiments on C6 glioma cells revealed the origin of the obtained current signals to be dominated by the flow of Na^+ and K^+ ions through their respective voltage-gated channels, since the electrical activity can be effectively abolished using appropriate pharmacological ion channel inhibitors. Moreover, we observed pronounced current fluctuations in the signals obtained from glioma cells. Given the technical setup of measuring several hundreds of thousands cells as a single population, we presume that these observed current oscillations must be happening in a concerted and likely a functional manner, at least across a sufficient number of cells at the same time, to become detectable. Thus, individually electrically active glioma cells can coordinate continuous and diverse electric responses in the picoampere-range throughout large cell populations.
The analysis of bioelectronic activity of cells was done in time and frequency representation. For the spectral analysis, we calculated the power spectral density function S_I from the obtained current signals. In glioma cells, the S_I scaled with $1/f^\gamma$, where in most cases $1.5 \leq \gamma \leq 2$. Hence, we identified the current noise of cells to be composed of firstly a 'baseline' thermal noise, related to constant operation of ion pumps in the cell membrane due to metabolic physiological activity. Secondly, overlaying low-frequent processes, that are related to functional events like fast release of ions through membrane ion channels, exhibit a much higher spectral magnitude in the frequencies below 10 Hz.

In a long-term recording of murine primary hippocampal neurons over 2 weeks, we observed the evolution of bioelectronic activity from an isolated *single cell behavior* towards a neuronal network communication. For the study of signal evolution, we introduced the method of spectrogram to achieve a time-resolved spectral analysis of the recorded signals. Hence, we observed and depicted examples of remarkable bioelectronic activity.
The magnitude of random current noise fluctuation at the beginning decreased within the measuring period and could be found only sporadically in the signals at the end of the experiment. Within the recorded signals, we found numerous regions which feature low frequent current oscillations, that were mostly periodic and of huge magnitudes. With time, the magnitude of these intensely pronounced patterns even increased up to 150 nA. We assume that such low frequent waves are highly functional and result from a collaborative,simultaneous and synchronous bioelectronic activity of an enormous number of neurons in the transducer. For establishing such a high degree of collaborative behavior, the neurons have to connect to each other

and build up a neuronal network communication. In fact, the neurons established a high degree of network connections on the transducer, which were observed with optical microscopy. The fresh, embryonic neurons colonized on the transducer and formed a complex neuronal network.

The success of generating neuronal networks *in vitro* on our transducer allows us to investigate the neuronal network behavior in the future. We are interested to study different aspects and processes regarding collaborative neuronal network activity, especially in the field of *learning and memory* in the human brain, but also the effects of for example different anesthetics or drugs. All of these questions are related to collaborative processes within highly complex neuronal networks.

With our setup, we present a tool for precise measurements of bioelectronic activity of cell populations as an *in vitro* reference for studying overall electrophysiological properties of cell networks *in vivo*.

In the future, we hope to support the improvement and the ongoing progress of modern medicine to ultimately help people, who suffer from neurological dysfunctions. Therefore, with this amazing project, we will pursue the actual research in neuroscience to better *Understand Cells Communication*.

7 Acknowledgments

References

[1] ROCHA, P. R. F. ; SCHLETT, P. ; SCHNEIDER, L. ; DROGE, M. ; MAILANDER, V. ; GOMES, H. L. ; BLOM, P. W. M. ; LEEUW, D. M.: Low frequency electric current noise in glioma cell populations. In: *J. Mater. Chem. B* 3 (2015), S. 5035–5039. `http://dx.doi.org/10.1039/C5TB00144G`. – DOI 10.1039/C5TB00144G

[2] KANDEL, Eric R. ; SCHWARTZ, James H. ; JESSELL, Thomas M. u. a.: *Principles of neural science*. Bd. 4. McGraw-Hill New York, 2000

[3] BIER, Martin: How to Evaluate the Electric Noise in a Cell Membrane? In: *ACTA PHYSICA POLONICA SERIES B* 37 (2006), Nr. 5, S. 1409

[4] WOLFE, Richard A. ; SATO, GH ; MCCLURE, DB: Continuous culture of rat C6 glioma in serum-free medium. In: *The Journal of cell biology* 87 (1980), Nr. 2, S. 434–441

[5] NYQUIST, H.: Thermal Agitation of Electric Charge in Conductors. In: *Phys. Rev.* 32 (1928), Jul, 110–113. `http://dx.doi.org/10.1103/PhysRev.32.110`. – DOI 10.1103/PhysRev.32.110

[6] COUCH, II ; LEON, W: *Digital and analog communication systems*. Prentice Hall PTR, 1990

[7] LIU, Qingjun ; WU, Chunsheng ; CAI, Hua ; HU, Ning ; ZHOU, Jun ; WANG, Ping: Cell-Based Biosensors and Their Application in Biomedicine. In: *Chemical Reviews* 114 (2014), Nr. 12, 6423-6461. `http://dx.doi.org/10.1021/cr2003129`. – DOI 10.1021/cr2003129. – PMID: 24905074

[8] RIVNAY, Jonathan ; OWENS, Róisín M ; MALLIARAS, George G.: The rise of organic bioelectronics. In: *Chemistry of Materials* 26 (2013), Nr. 1, S. 679–685

[9] THOMAS, C.A. ; SPRINGER, P.A. ; LOEB, G.E. ; BERWALD-NETTER, Y. ; OKUN, L.M.: A miniature microelectrode array to monitor the bioelectric activity of cultured cells. In: *Experimental Cell Research* 74 (1972), Nr. 1, 61 - 66. `http://dx.doi.org/http://dx.doi.org/10.1016/0014-4827(72)90481-8`. – DOI http://dx.doi.org/10.1016/0014–4827(72)90481–8. – ISSN 0014–4827

[10] JONES, IanL. ; LIVI, Paolo ; LEWANDOWSKA, MartaK. ; FISCELLA, Michele ; ROSCIC, Branka ; HIERLEMANN, Andreas: The potential of microelectrode arrays and microelectronics for biomedical research and diagnostics. In: *Analytical and Bioanalytical Chemistry* 399 (2011), Nr. 7, 2313-2329. `http://dx.doi.org/10.1007/s00216-010-3968-1`. – DOI 10.1007/s00216–010–3968–1. – ISSN 1618–2642

[11] RAMMELT, U. ; REINHARD, G.: On the applicability of a constant phase element (CPE) to the estimation of roughness of solid metal electrodes. In: *Electrochimica Acta* 35 (1990), Nr. 6, 1045 - 1049. http://dx.doi.org/http://dx.doi.org/10.1016/0013-4686(90)90040-7. – DOI http://dx.doi.org/10.1016/0013–4686(90)90040–7. – ISSN 0013–4686

[12] MELO, LL ; VAZ, AR ; SALVADORI, MC ; CATTANI, M: Grain sizes and surface roughness in platinum and gold thin films. In: *Journal of Metastable and Nanocrystalline Materials* Bd. 20 Trans Tech Publ, 2004, S. 623–628

[13] GABOR, D.: Theory of communication. Part 1: The analysis of information. In: *Electrical Engineers - Part III: Radio and Communication Engineering, Journal of the Institution of* 93 (1946), November, Nr. 26, S. 429–441. http://dx.doi.org/10.1049/ji-3-2.1946.0. – DOI 10.1049/ji–3–2.1946.0

[14] BLISS, Tim V. ; COLLINGRIDGE, Graham L. u. a.: A synaptic model of memory: long-term potentiation in the hippocampus. In: *Nature* 361 (1993), Nr. 6407, S. 31–39

[15] KANDEL, Eric R.: The molecular biology of memory storage: a dialogue between genes and synapses. In: *Science* 294 (2001), Nr. 5544, S. 1030–1038

[16] KANDEL, Eric R. ; SCHWARTZ, James H.: Molecular biology of learning: modulation of transmitter release. In: *Science* 218 (1982), Nr. 4571, S. 433–443

[17] BEAR, Mark F. ; MALENKA, Robert C.: Synaptic plasticity: LTP and LTD. In: *Current Opinion in Neurobiology* 4 (1994), Nr. 3, 389 - 399. http://dx.doi.org/http://dx.doi.org/10.1016/0959-4388(94)90101-5. – DOI http://dx.doi.org/10.1016/0959–4388(94)90101–5. – ISSN 0959–4388

[18] ALBENSI, Benedict C. ; OLIVER, Derek R. ; TOUPIN, Justin ; ODERO, Gary: Electrical stimulation protocols for hippocampal synaptic plasticity and neuronal hyper-excitability: Are they effective or relevant? In: *Experimental Neurology* 204 (2007), Nr. 1, 1 - 13. http://dx.doi.org/http://dx.doi.org/10.1016/j.expneurol.2006.12.009. – DOI http://dx.doi.org/10.1016/j.expneurol.2006.12.009. – ISSN 0014–4886

[19] CLUGNET, MC ; LEDOUX, JE: Synaptic plasticity in fear conditioning circuits: induction of LTP in the lateral nucleus of the amygdala by stimulation of the medial geniculate body. In: *The Journal of Neuroscience* 10 (1990), Nr. 8, 2818-2824. http://www.jneurosci.org/content/10/8/2818.abstract
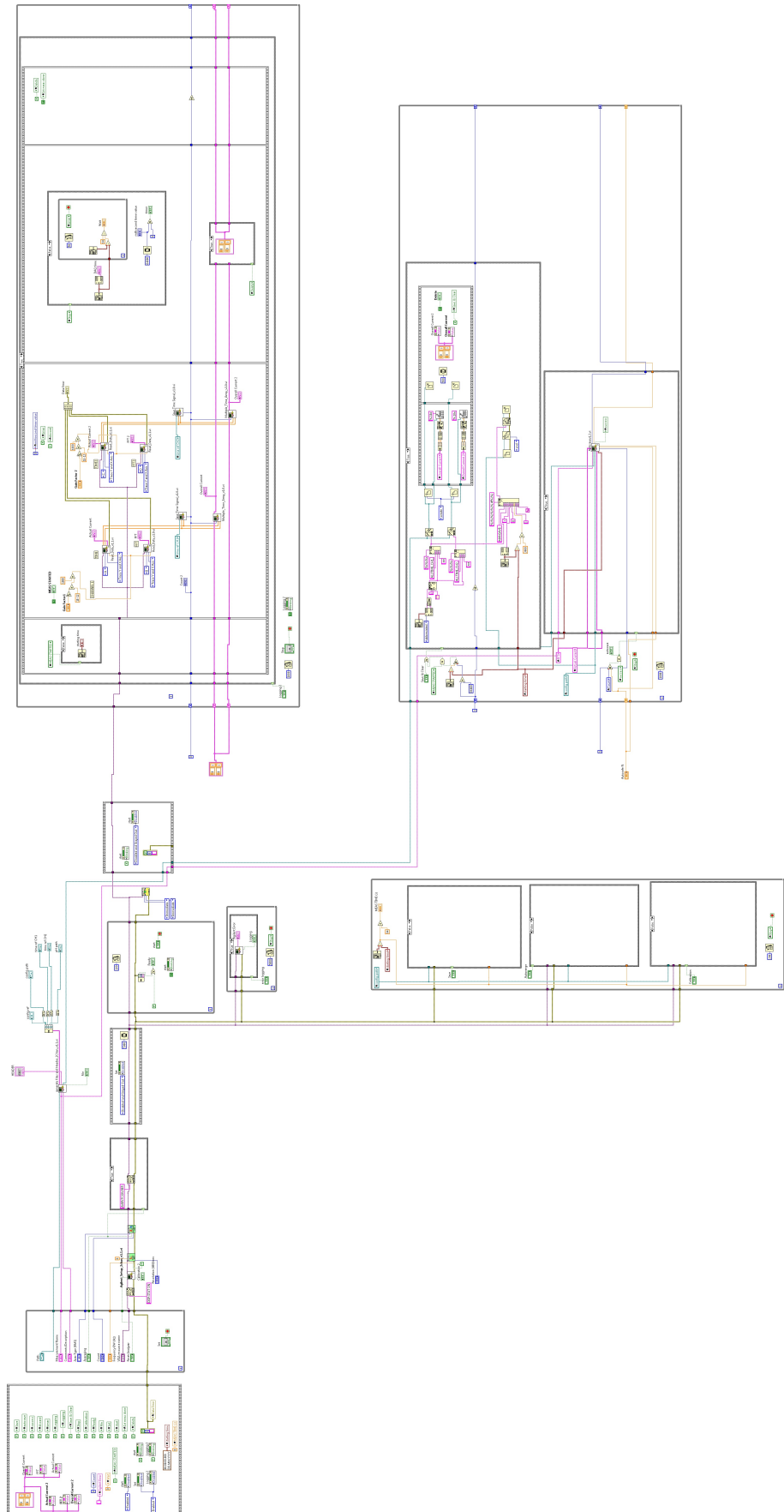
Appendix

I LabVIEW source code (overview Main VI)

II Neuron medium preparation and extraction protocol

Medium Preparation:

Plating Medium	50ml	100ml
MEM+Glutamax	40.5	86
15%Horse Serum	7.5	15
20%Glucose	1.5	3
PS(penicillin streptomycin	0.5	1

Full Neurobasal media	50ml	100ml
Neurobasal or Neurobasal-A Medium/ml	48,375	96,75
B-27 Supplement/ml	1	2
L- Glutamin(1% glutamax)/ml	0,125	0,25
PS/ml	0,5	1

Filter,PH=7.4

Primary neuronal cell culture for chips

1. Coating plates with **0.5mg/ml** PLL(poly-L-lysine) overnight at 4degree,or 5h at 37degree

2. Wash 3 times with **plating medium** carefully,

3. Add plating medium 250ul in each chip, keep in37℃, CO2 incubator

4. Hippocampus dissection

5. suck off the supernatant from the hippocampus,

6. wash twice with 5mL MEM,

7. Add 300 ul Trypsin end in 5ml MEM,37℃water bath for 12 min(after 5 min check every min)

8. prepare fire polished pipettes

9. add some **plating medium** to stop over-digestion, suck off the supernatant and add 3ml **plating medium**

10. Perform tissue trituration with glass pipette（10times,slightly to avoid bubble,

11. suck out the supernatant to another tube

12. count cells

13. seed 400,000cells -----*transfer 400,000cells to a 1.5ml Eppendorf tube and add some fresh plating medium end in 800ul, dispersed well in advance*

14. After 3h incubation in plating medium, wash1 x per-warm PBS, incubate with 800ul **NBA/full (+B27)** per chip.
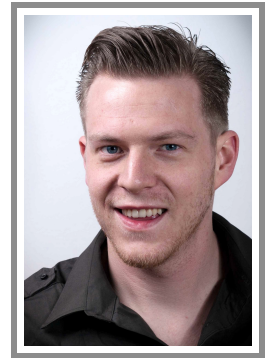
Note: change medium every day.

Eigenständigkeitserklärung

Ich versichere, die vorliegende Arbeit selbstständig unter der Anleitung des Referenten und Korreferenten durchgeführt und nur die angegebenen Referenzen und Hilfsmittel benutzt zu haben.

Mainz,
12. August 2015

Paul Schlett

✉ paul.schlett@googlemail.com

Education

since 08/2011   **Student of Applied Physics (M.Sc.)**,
Hochschule RheinMain, University of Applied Science, Rüsselsheim, Germany.
Masterthesis: Understanding cells communication - low frequency electric current measurements of cell populations, Max-Planck-Institute for Polymer Research, Mainz, Germany. *anticipated date of graduation: September 2015*

05/2007–07/2011   **Bachelor of Science (B.Sc.) Physical Engineering**,
Hochschule RheinMain, University of Applied Science, Rüsselsheim, Germany, *Final Grade 1.1 (with distinction)*.
Bachelorthesis: Development of a artificial cardiovascular Simulator. Grade: 1.0

03/2006   **Higher education entrance qualification**, *Gymnasium Gonsenheim*, Mainz, Germany, *Final grade 1.8*.

Experience

03/2013–03/2014   **Assistent Lecturer**, *Hochschule RheinMain, University of Applied Science*, Rüsselsheim, Germany.
Instructor/Tutor for several courses (for Bachelor degree-students):
- CAD (SolidWorks, ST 2013)
- Measurement Data Acquisition and Processing (LabVIEW, Summer term 2013 and winter term 2013/14)
- Technical Physics 1 & 2 (Winter term 2014/15)

since 01/2013   **Field Engineer**, *Cardioskills GmbH & Co. KG*, Frankfurt am Main, Germany.
Instructor/ Field Engineer for medical trainings:
- Set-up and check of medical simulators (Cathlab, Simbionix)
- Supervision of courses
- Technical support during courses

08/2011–04/2012   **Project Engineer**, *Hochschule RheinMain, University of Applied Science*, Rüsselsheim, Germany.
Biomedical Measurements & Signal Processing Laboratory,
Director Prof. Dr. A. Brensing
Project: Cardiovascular simulator MACSim, main tasks:
- Validation of the simulator and measurement data analysis
- Constructive improvement of the simulator and software
- Project documentation

03/2010–03/2011   **Internship**, *Hochschule RheinMain, University of Applied Science*, Rüsselsheim, Germany.
Biomedical Measurements & Signal Processing Laboratory,
Director Prof. Dr. A. Brensing
Project: Cardiovascular simulator MACSim, main tasks:
- Design and construction of the entire simulator
- Purchase of all components
- Assembly of the simulator and functional testing

Publications

03/2015 **Monitoring brain cells for investigation of cell communication - In-vitro low frequency electric current measurements on neuronal networks**,
Paul Schlett, Paulo Rocha, Paul Blom, Dago de Leeuw,
BioEl 2015 International Winterschool on Bioelectronics, Kirchberg, Austria,
Poster presentation.

03/2015 **Low frequency electric current noise in glioma cell populations**,
P.R.F. Rocha, P. Schlett, L. Schneider, M. Dröge, V. Mailänder, H.L. Gomes, P.W.M. Blom, D.M. de Leeuw,
J. Mater. Chem. B 3, *2015, DOI10.1039/C5TB00144G.*

09/2012 **Herz-Kreislauf-Simulator**, *P. Schlett, A. Brensing, S. Bernhard,*
MED Engineering, Hanser-Verlag, 2012, Germany.

09/2011 **Herz-Kreislaufsimulator MACSim**, *P. Schlett,*
Annual Conference of The German Society for Biomedical Engineering within VDE, Freiburg, Germany, *Poster presentation.*

09/2011 **Herz-Kreislauf-Simulator MACSim**, *P. Schlett, A. Brensing, S. Bernhard,*
Virtuelle Instrumente in der Praxis 2011: Begleitband zum 16. VIP-Kongress, *VDE-Verlag, Germany*, 2011.

Languages

German | mother tongue
English | fluent
French | beginner

Computer Skills

NI LabView | professional skills
Basic Course "LabView Core 1" (3 days)
Certified LabView Associate Developer (CLAD-Certificate)

Matlab | professional skills
SolidWorks (CAD) | Advanced skills
MS-Office | Advanced skills
EAGLE | Basic skills

Miscellaneous

since 03/2011 | Scholarship holder from *Studienstiftung des deutschen Volkes*

Winter term 2007/08 and Summer term 2008 | exemption from duties and taxes of the Hochschule RheinMain due to excellent grades

Personal Interests

Music | Drummer in band (Rock), music production (Recording, Mixing)
Travel | Canada, Nepal, Indonesia
Misc. | Photography, Diving

August 8, 2015